

An Elemental Modelling Method for Linear Motor Parametric Studies Using Boundary-Free Analytic Magnetic Field Solutions: Including 3D Geometry, Permeability, and End Effects

Matthew Forbes^{a,*}, William S. P. Robertson^a, Anthony C. Zander^a, Johannes J. H. Paulides^b

^a*The University of Adelaide, North Terrace, Adelaide, 5005, SA, Australia*

^b*Advanced Electromagnetics Group, Industrieweg 78, Waalwijk, 5145 PW, The Netherlands*

Abstract

In this article we highlight an Elemental Modelling Method, as an alternative to the standard Harmonic (or Fourier) Model, that can include variable permeability and non-periodic 3D geometry with superposition of boundary-free analytic magnetic field solutions. The methodology is demonstrated with an exhaustive parametric search to optimise a set of tubular double-sided Halbach slotless permanent magnet linear synchronous motor topologies, within a fixed volume constraint. The modelling method is computationally efficient, facilitating the search of close to 900,000 topologies with an axisymmetric-2D assumption, subsequently converted to a full 3D design. The aim of this study is to investigate the effect of strategic addition of iron within the topologies, against the trade-off of reducing permanent magnet volume – such an analysis is not simple, or possible, within the Harmonic Model. The elements of the model include coil filaments, permanent magnets, and iron segments inclusive of saturation effects from nonlinear permeability. A design with inset permanent magnets and surface iron found in the parametric search is shown to outperform the optimal Halbach topologies, with improved figures of merit for force and force ripple with low phase currents. Results are compared with Finite Element Analysis and performance of a design with non-unity relative permeability of the permanent magnets is assessed.

Keywords: Magnetic field modelling, Exact analytical solution, Magnetostatics, Linear synchronous motor, Nonlinear magnetic materials, Semi-analytic forces

1. Introduction

Traditionally, an analytic description of the magnetic field in linear (and electric) motors is found using the Harmonic Model (or Fourier Model), which divides the motor into discrete regions with plane boundary conditions [1, 2, 3, 4]. The Harmonic model uses separation of variables to solve the fundamental differential equations, derived from Maxwell's equations: the homogeneous Laplace equation in vacuum (or a source-free region) and the inhomogeneous Poisson equation in matter (coil, magnet, iron). This process generates an orthogonal set of (coordinate-dependent) functions with expansions given as periodic Fourier series [5, pg.508], [6]. The Fourier coefficients are used to describe the magnetic sources (magnetisation, current) in each region that vary spatially along the motor axis: a multipole expansion or multiphase coil. It is not possible to programmatically find a suitable model for any linear motor using the Harmonic Model, as one may do in Finite Element Analysis (FEA) with close-to complete freedom; this places limits on the ability to solve for the field with arbitrary geometry and placement of iron, coils, and permanent magnets (PMs). This is a common trade-off for analytic solutions, where assumptions are applied to formulate the problem, yet such solutions

can provide significant computational advantage over numerical methods with minimal discrepancy.

Instead of using separation of variables to solve such problems, the alternate analytic modelling approach is to use Green's functions to solve the differential equations [7, §3]. This method provides integral formulations for the unbounded magnetic field from coils or permanent magnets, under the assumptions they retain their geometry, and have a constant and uniform magnetisation or current that is unaffected by self or external fields (rigid, linear, homogeneous). The benefit of a Green's function approach over the Harmonic Model is non-periodic effects (higher-order harmonics, end-effects) are intrinsically captured and permanent magnets and coils can be freely added or removed from the model, without loss of generality, due to the principle of superposition. However, the challenges preventing adoption have been:

- the availability and complexity of elemental analytic solutions;
- the inclusion of nonlinear material permeability;
- an efficient and accurate algorithm to calculate force and torque.

There have been recent advances in all three areas that have made this feasible.

*Corresponding author

Email address: matthew.forbes@adelaide.edu.au (Matthew Forbes)

Elemental analytic magnetic field solutions are contingent on geometry and the magnetisation or current direction, and typically can only be found assuming unity relative permeability. The magnetic field of a polyhedron with any uniform magnetisation vector is known, and any shape with plane boundaries can be formed with polyhedra [8, 9, 10] and cuboids [11]. To directly model curved surfaces, there are more complex solutions for the principal magnetisation directions (radial, diametric, azimuthal, axial) of rectangular cylindrical permanent magnets [12, 13, 14, 15, 16] and coils with various current densities [12, 17, 18, 19]. This collection forms all typical geometric elements in a linear motor; however, superposition of solutions cannot be applied in a model with nonlinear elements. A linearisation process is outlined and demonstrated in [20, 21], that can discretise iron segments, using a nonlinear single-line equivalent B - H curve, into a set of permanent magnets with principal magnetisations. This process effectively captures saturation effects from material properties and geometry, something not possible in the Harmonic Model under the typical infinite permeability boundary condition. Finite permeability and slots in the Harmonic Model require a Permeance Model [22] or hybrid approach — for example, with Magnetic Equivalent Circuit [23], Anisotropic Layer Theory [24], or Schwarz-Christoffel Mapping [25, 26] — or otherwise an extension into a Subdomain Model [27]; however, these methods are generally limited to 2D.

Due to a large set of elements in the model combined with the complexity of the analytic solutions, it is not feasible to find analytic force and torque solutions (integration of the field functions) between all the permutable combinations of the permanent magnets and coils. Thus, semi-analytic solutions are required, especially since potential closed-form analytic force solutions would not include non-unity relative permeability. Similar to the Harmonic Models, an electromagnetic stress tensor can be used to avoid the computationally expensive local meshing of magnetic field sources [28]. The classical Maxwell Stress Tensor introduces significant error into the calculation from the field discretisation (and error from using a finite sum of an exact series solution [12, 19, 29]), with a new generalised form able to rectify prior issues [21].

In this article numerous double-sided linear motor topologies are analysed using a new method, reducing the number of assumptions required to form an analytic model, that increases solution accuracy. This is on the proviso that analytic magnetic field solutions are known for all model elements. Whence, there are no limiting requirements of: geometric symmetry; material properties with infinite or constant relative permeability; plane spatial boundary conditions. A parametric study using this new method is performed with results compared to literature that uses the traditional Harmonic Model. Unique augmentations are made to the classical motor topologies (Halbach, axial, and radial magnetisation) in 2D and 3D, demonstrated for the first time within an analytic framework. The new methodology in the article can be readily extended to rotary drives.

In Section 2, steps required to implement the Elemental Modelling Method for both linear and nonlinear models are described. In Section 3, three approaches are outlined towards

calculating the force in a linear motor, depending on the physical description of the coil array and location at which the force is calculated. In Section 4, a motor paradigm is introduced as the application focus of this article, along with a review of (and comparison to) the literature that has previously modelled this design using the Harmonic Model. In Section 6 a comparative study is performed between different motor topologies, modelling various inclusions of iron into the canonical designs with the aim of finding a design that can provide an increase to force from of an ironless Halbach array, without introducing additional force ripple. Capability of the method to convert a design from an axisymmetric 2D model to an exact 3D model is shown, as well as effectively including nonlinearities from both iron and permanent magnets, with results shown to closely match FEA in Section 6.3.

2. Elemental modelling method

The elemental (or non-periodic) modelling method comprises exact 3D analytic magnetic field solutions with a unity relative permeability. With cylindrical structures, these field solutions have degenerate solutions with special cases such as axisymmetry (cylindrical arc to ring). Permanent magnets are modelled in integral form using the (mathematically equivalent) Current Model or Charge Model (with magnetisation A/m) [30, pgs. 184, 242], and coils are modelled in integral form using a Filament Model (or Biot-Savart) (with currents: 0D A, 1D A/m, 2D A/m²) [7, §3], [12, §A]; the combination of these elements forms a motor model.

The general procedure to model force and torque in a motor is summarised in Figure 1 and detailed below. A repository demonstrating basic force and torque calculations, using a compendium of analytic field solutions, is available at [31]. An algorithm for mathematical implementation of the method can be found in [21, §A].

1. For a known analytic solution, assign the coil and permanent magnet: geometry, location, and magnetisation or current. If there is no permeable matter ($\mu_r = 1$), then skip to Step 6.
2. Calculate the total magnetic flux density (\mathbf{B}) from all coils and permanent magnets with unity relative permeability across the regions with permeable matter ($\mu_r \neq 1$ regions assumed vacuum). For nonlinear permanent magnets this includes the base linear magnetic remanence, with field calculated through the volume, including the internal field. Discretise the permeable regions into volumes (geometry, location), defining the total magnetic flux density (\mathbf{B}_0) at each centroid.
3. Using \mathbf{B}_0 and the B - H curve for the permeable material, assign an initial uniform vector magnetisation to each volume element with $\mathbf{M} = (\mu_r - 1)\mathbf{H}$. For a cylindrical volume element, this magnetisation can be split into the superposition of the principal magnetisations $\mathbf{M} = M_\perp(\cos\varphi^*\mathbf{e}_x + \sin\varphi^*\mathbf{e}_y) + M_\rho\mathbf{e}_\rho + M_\varphi\mathbf{e}_\varphi + M_z\mathbf{e}_z$. The effect of laminations, or a preferred direction of magnetisation, can be modelled by weighting or removing basis

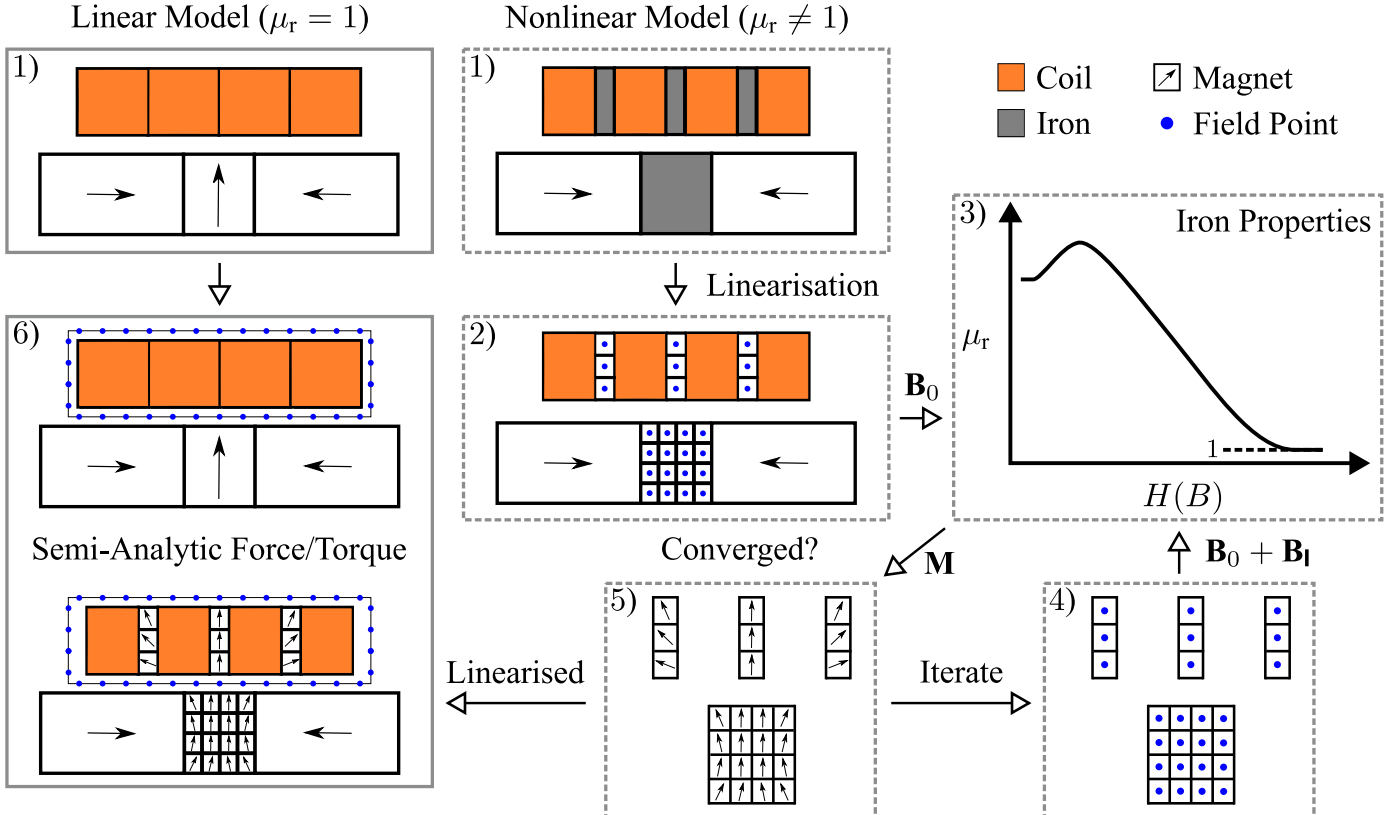


Figure 1: Field points for calculation of the magnetic flux density to linearise a nonlinear model and/or give the force and torque between two arbitrary collections of permanent magnets and coils. An iterative process is used to find an equivalent set of permanent magnets that model the magnetisation of the permeable iron. The process has generalised Steps 1-6 as detailed in Section 2.

vectors, e.g. $H_z = M_z = 0$. For nonlinear permanent magnets, these magnetisations are superimposed, yet are now independent, to the original remanent magnetisation (an example is given in Figure 14c). An algorithm for this step is shown in [21, §A]

4. Calculate the total magnetic flux density from all new volume elements or ‘equivalent permanent magnets’ (\mathbf{B}_l), including the self-field, at all centroids defined in Step 2. The field \mathbf{B}_0 does not change.
5. Follow the same process of Step 3, assigning new magnetisations with $\mathbf{B}_0 \rightarrow \mathbf{B}_0 + \mathbf{B}_l$. If convergence criteria are met, e.g. minimal magnetisation change, then proceed to Step 6. Otherwise, repeat Step 4, calculating the magnetic flux density at all centroids. This step should be repeated – continually recalculating the magnetising field from the permeable regions with iteratively changing magnetisations. This iteration takes longer for regions with higher relative permeabilities.
6. Form a closed-surface in the airgap ($\mathbf{B} = \mu_0 \mathbf{H}$) around either the stator or rotor/mover volume. Mesh the surface and calculate the discretised magnetic field at each area centroid from all sources (permanent magnets, coils, ‘iron’) external \mathbf{B}_E and internal \mathbf{B}_I to the surface. Calculate the force $\mathbf{F}_{GMST}(\mathbf{B}_E, \mathbf{B}_I)$ and torque $\mathbf{T}_{GMST}(\mathbf{r}, \mathbf{B}_E, \mathbf{B}_I)$ using the Generalised Maxwell Stress Tensor approach (Appendix A), with the local surface normal, area, radii,

and field.

As the model has a complete description of the field, it can be extended in future work to dynamic effects such as: eddy-currents in the conductor, iron, supporting structural components, and magnets; hysteresis; or back-EMF in the coils [32]. Use of the method can be extended to applications beyond force and torque, such as considering vibrations from eccentricity [33], or vibration and acoustics from electromechanical coupling [34, 35]. Eddy current, excess and hysteresis losses can be considered negligible in low frequency linear motor applications [36] when not considering the switching frequency of the inverter: assuming the relative permeability is not a function of frequency, the permeable matter is instantaneously magnetised and demagnetised not considering losses.

3. Cylindrical linear motor force

In this article there are two potential methods to calculate the summation of the forces using analytic magnetic field solutions on a coil array, depending on the physical interpretation: with current density ‘blocks’ (Section 3.1) or with filament currents that have an infinitesimal cross-section (Section 3.2). The advantage with the latter case, is that the axial force can be calculated analytically if the magnetic flux density over each coil filament is axisymmetric. However, with a large number of model elements (magnets, coils, iron segments) and 3D fields, it

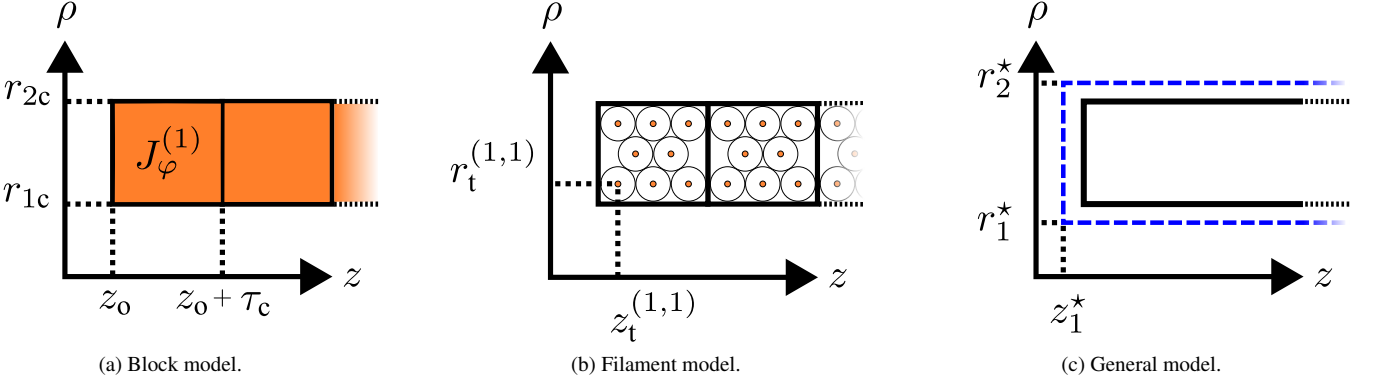


Figure 2: Basic axisymmetric-2D cylindrical parameterisation of the models in Section 3: (a) a solid coil with the external magnetic field (\mathbf{B}_E) calculated through the volume; (b) current filaments with \mathbf{B}_E calculated along a sum of contours; (c) any collection of magnetic elements, abstracting the force calculation to a closed-surface in the air-gap, using the internal magnetic field \mathbf{B}_I and \mathbf{B}_E .

is computationally efficient to use a general airgap mesh (Section 3.3), as opposed to calculating the magnetic flux density directly across the current density. Each model is visualised in Figure 2 along with a basic parameterisation that is used in each section.

3.1. Block model

The macroscopic Lorentz force

$$\mathbf{F}_L = \int_V \mathbf{J} \times \mathbf{B}_E \, dv \quad (1)$$

acts on a volumetric current density \mathbf{J} due to a superposition of all external field sources \mathbf{B}_E (excluding those from \mathbf{J}). For a cylindrical linear motor with azimuthal current J_φ ($A \cdot m^{-2}$), the axial Lorentz force simplifies to only requiring the radial component of the external magnetic flux density B_ρ (T)

$$F_z(\mathbf{r}) = - \int_V J_\varphi(\mathbf{r}) B_\rho(\mathbf{r}) \, dv, \quad (2)$$

from $(\mathbf{e}_\varphi \times \mathbf{e}_\rho) \cdot \mathbf{e}_z$ with cylindrical coordinates $\mathbf{r}(\rho, \varphi, z)$ and basis vectors $(\mathbf{e}_\rho, \mathbf{e}_\varphi, \mathbf{e}_z)$. If the cylindrical linear motor is axisymmetric in geometry, magnetic field, and current, then (1) reduces to a surface integral over some number n_c of discrete coils (or phases)

$$F_z = -2\pi \sum_{j=1}^{n_c} J_\varphi^{(j)} \int_{z=z_0+\tau_c(j-1)}^{z_0+\tau_c(j)} \int_{\rho=r_{1c}}^{r_{2c}} \rho B_\rho(\mathbf{r}) \, d\rho dz, \quad (3)$$

where each coil is assumed to have a uniform azimuthal current density and peak current \hat{J}_φ , between radii $[r_{1c}, r_{2c}]$ along length τ_c (m). For a three-phase commutation, the coil currents are

$$J_\varphi^{(j)} = \hat{J}_\varphi \sin\left(\frac{\pi}{\tau_p}(\phi_z + z_0) + (j-1)\frac{\pi}{3}\right), \quad (4)$$

scaled by an axial offset z_0 (m) of the coil array, and a phase alignment ϕ_z (m) to ensure peak current occurs between the poles with pitch τ_p (m). Equation (3) is simple to model in FEA or with the Harmonic Model, and \hat{J}_φ can be scaled by a packing factor term to account for discrete coil turns.

3.2. Filament model

If each coil is comprised of wires with small diameters in a region with a low magnetic field gradient $(\nabla \mathbf{B})^\top \cdot \mathbf{e}_\rho$, then we can assume B_ρ is uniform across each discrete coil turn n_t , within each coil phase. Locally the gradient is zero, yet the field will change between adjacent coil turns. With this assumption the current density locally reduces to a current loop (filament) $I_\varphi = J_\varphi \int d\rho dz$ with unit A, with the integral now independent to $\rho B_\rho(\mathbf{r})$. It follows from (3) that B_ρ will only need to be calculated n_t times for each coil, at a point along the contour of the current loop $\mathbf{r}_t(\rho, z)$ with radii r_t :

$$F_z = 2\pi \sum_{j=1}^{n_c} \frac{J_\varphi^{(j)} \tau_c(r_{1c} - r_{2c})}{n_t} \sum_{k=1}^{n_t} r_t^{(j,k)} B_\rho(\mathbf{r}_t^{(j,k)}). \quad (5)$$

The filament assumption removes the integral and gives an analytic solution, given $B_\rho(\mathbf{r})$. With a rectangular grid of many coil turns \mathbf{r}_t (filaments), Equations (3) and (5) will give almost identical solutions [§5.2]. As each coil turn also maps to one filament, (5) provides the capability to model unique winding patterns and capture changes to the force profile from discrete coil turn placements.

It may be reasonable to find optimal topologies of an actuator design assuming axisymmetry; however, due to limitations in manufacturing of geometries, tolerances, and/or magnetisations, there is likely to be a 3D radial magnetic flux distribution. An example is ‘approximating’ ring magnets using cuboidal magnets [37], or radial magnetisation with diametrically magnetised arcs [38]. For an extension to include 3D geometries with a non-axisymmetric magnetic field, the evaluation of (5) requires a sum of contour integrals

$$F_z = \sum_{j=1}^{n_c} \frac{J_\varphi^{(j)} \tau_c(r_{1c} - r_{2c})}{n_t} \sum_{k=1}^{n_t} r_t^{(j,k)} \int_{\varphi=0}^{2\pi} B_\rho(\mathbf{r}_t^{(j,k)}) \, d\varphi. \quad (6)$$

If there is no analytic solution to the integral, the semi-analytic solution with a linearly spaced mesh along the contour is

$$F_z = 2\pi \sum_{j=1}^{n_c} \frac{J_\varphi^{(j)} \tau_c(r_{1c} - r_{2c})}{n_t} \sum_{k=1}^{n_t} \frac{r_t^{(j,k)}}{N} \sum_{l=1}^N B_\rho(\mathbf{r}_t^{(j,k,l)}). \quad (7)$$

The number of field point calculations N along each contour is increased until the axial force converges.

3.3. General model

By inspection of (7), a computational burden can be envisaged if the model has a large number of filaments (that each need to be discretised) and/or a large number of external magnetic field sources. The standard Lorentz form (1) using a Filament Model (5, 7) only includes the force on the coils, and the local semi-analytic meshing is complicated by additional magnetic field sources, such as slots in the coils or permanent magnets. The solution is to abstract the field discretisation away from the source locations into the air-gap between the mover and stator. This is done using the Generalised Maxwell Stress Tensor $\mathcal{F}(\mathbf{B}_E(\mathbf{r}), \mathbf{B}_I(\mathbf{r}))$ (Appendix A)

$$\mathbf{F}_{GMST}(\mathbf{B}_E, \mathbf{B}_I) = \int_V \nabla \cdot \mathcal{F}(\mathbf{B}_E, \mathbf{B}_I) dV = \oint_{\partial V} \mathcal{F}(\mathbf{B}_E, \mathbf{B}_I) \cdot \mathbf{n} ds, \quad (8)$$

where \mathbf{B}_I is a superposition of field sources internal to the closed surface ∂V , and the divergence (or Lorentz form) with force density \mathbf{f}_L is

$$\begin{aligned} \mu_0 \nabla \cdot \mathcal{F}(\mathbf{B}_E, \mathbf{B}_I) &= \nabla \cdot [\mathbf{B}_E \otimes \mathbf{B}_I + \mathbf{B}_I \otimes \mathbf{B}_E - (\mathbf{B}_E \cdot \mathbf{B}_I) \mathcal{I}] \\ &= (\nabla \times \mathbf{B}_E) \times \mathbf{B}_I + (\nabla \times \mathbf{B}_I) \times \mathbf{B}_E \\ &\quad + \mathbf{B}_I(\nabla \cdot \mathbf{B}_E) + \mathbf{B}_E(\nabla \cdot \mathbf{B}_I) \end{aligned} \quad (9)$$

where \mathcal{I} is the identity tensor. Equation (8) has a linearly increasing computational expense with increasing elements (magnets, coils, iron segments), and is favourable over the local discretisation in (7).

Applying the parameterisation from (3) to (8) gives four surfaces that enclose the coil array

$$\begin{aligned} F_z &= \sum_{s=1}^2 (-1)^s \left[r_s^* \int_{z=z_s^*}^{z_s^*} \int_{\varphi=0}^{2\pi} \left([\mathcal{F}(\mathbf{B}_E, \mathbf{B}_I) \cdot \mathbf{e}_\rho] \cdot \mathbf{e}_z \right) \Big|_{r_s^*} d\varphi dz \right. \\ &\quad \left. + \int_{\varphi=0}^{2\pi} \int_{\rho=r_1^*}^{r_2^*} \rho \left([\mathcal{F}(\mathbf{B}_E, \mathbf{B}_I) \cdot \mathbf{e}_z] \cdot \mathbf{e}_z \right) \Big|_{z_s^*} d\rho d\varphi \right] \end{aligned} \quad (10)$$

with radial and axial surface definitions of $r_s^* \in \{r_{1c} - \frac{a}{2}, r_{2c} + \frac{a}{2}\}$ and $z_s^* \in \{-\frac{a}{2}, n_c \tau_c + \frac{a}{2}\}$, where a is scaled to half the radial air gap. The semi-analytic solution to (10) is

$$\begin{aligned} F_z &= \frac{2\pi}{N_\varphi} \sum_{s=1}^2 (-1)^s \sum_{q=1}^{N_\varphi} \left[r_s^* \frac{z_2^* - z_1^*}{N_z} \sum_{n=1}^{N_z} (B_\rho^E B_z^I + B_z^E B_\rho^I)^{(n,q)} \Big|_{r_s^*} \right. \\ &\quad \left. + \frac{1}{2} \sum_{m=1}^{N_\rho} [(r^{(m)} + \Delta r)^2 - (r^{(m)} - \Delta r)^2] \right. \\ &\quad \left. \times (B_z^E B_z^I - B_\rho^E B_\rho^I - B_\varphi^E B_\varphi^I)^{(m,q)} \Big|_{z_s^*} \right], \end{aligned} \quad (11)$$

where $\Delta r = (r_2^* - r_1^*)/(2N_\rho)$ and $N_{\{\rho, \varphi, z\}}$ controls the number of field point calculations on each surface. All magnetic flux densities in (11) are calculated at shell $\mathbf{r} = r_s^* \mathbf{e}_\rho + \varphi^{(q)} \mathbf{e}_\varphi + z^{(n)} \mathbf{e}_z$

or disc $\mathbf{r} = r^{(m)} \mathbf{e}_\rho + \varphi^{(q)} \mathbf{e}_\varphi + z_s^* \mathbf{e}_z$ centroids in a rectangular cylindrical grid with $\mathbf{B}_E(\mathbf{r}) = B_\rho^E \mathbf{e}_\rho + B_\varphi^E \mathbf{e}_\varphi + B_z^E \mathbf{e}_z$ and $\mathbf{B}_I(\mathbf{r}) = B_\rho^I \mathbf{e}_\rho + B_\varphi^I \mathbf{e}_\varphi + B_z^I \mathbf{e}_z$. Returning to (3), for an axisymmetric field across the coils then substituting $N_\varphi = 1$ into (11) removes the q -summation, leaving a rectangular closed contour integral defined by the four points of r_s^* and z_s^* .

4. Permanent magnet linear synchronous motor topology and previous work

In this article we are modelling and performing a parametric study on a tubular double-sided Halbach array with a slotless moving coil, shown in Figure 3, using the elemental modelling method from Section 2 and general force model (11). This linear motor design first appeared in the literature in 2011 [39] with analytic permanent magnet field solutions using the Harmonic Model (later with a single-phase current density [40], and three-phase optimisation [41, §5]). Independently and also using the Harmonic Model, a complete field and force model with a design optimisation was given in 2012 [42] (summarised in [43]). Planar versions of this linear motor have been investigated using the charge and current models [44, 45]. This variation is also possible to model with elements, joining straight wire segments [46, pg. 225] and arc segments [12, §4.1] to create the ‘racetrack coil’, with cuboidal permanent magnets [11]. This was shown with the 3D field from a polygonal-shaped linear motor [37], and accurate force profiles can be found applying the Generalised Maxwell Stress Tensor (8).

The tubular linear motor has a geometrically ideal current density compared to certain planar topologies as there is reduced stray field from being ‘wrapped’ and there are no end-windings (only conductors to connect the various coils) – meaning nearly the entire coil contributes to force generation. The double-sided Halbach array is beneficial as there is minimal net ‘global’ attraction between the inner and outer shells, meaning reduced mass required from supporting structures, combined with the high energy density modern permanent magnets. When the coil is iron-less (air core), there are no passive and minimal active attraction forces to either side of the stator, further reducing supporting structures and issues with sliding Coulomb friction. All of these factors produce a compact, high force density motor per unit mass, which has the possibility of achieving precise position control and high acceleration without reluctance forces. To form the tubular linear motor, magnetic field solutions for 3D cylindrical arc or axisymmetric-2D ring permanent magnets are given in [12] for magnetisations: radial (§5.2); axial (§5.4); and, diametric (§5.1). Filaments are placed at the centroid of the wires with magnetic field solution in [12, §4.1].

The tubular structure is difficult to optimise due to radial flux asymmetry in the airgap (depending on the radius of curvature). The inner Halbach array weakens its own air-gap flux density, meaning an optimal force per unit mass is found when the motor has a large outer radius and is relatively hollow (a significant inner radius, e.g. $r_i > 0.5r_o$) [37]. The double-sided Halbach array also insulates the heat generated by the coils,

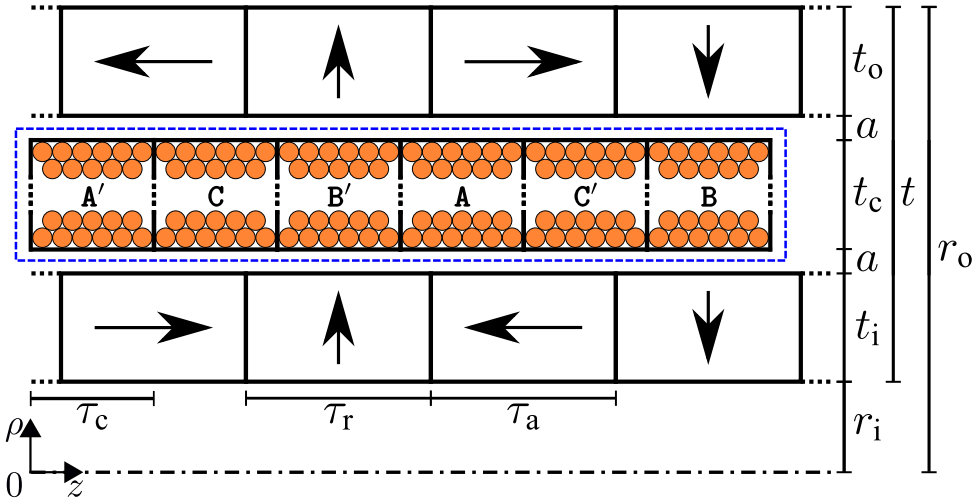


Figure 3: Cross-section and geometric parametrisation of a periodic segment of a double-sided Halbach motor. Fictitious coil wires are shown in orange with current densities from (4) of $\{A', C', B', A, C, B\} = \{J_\psi^{(1)}, J_\psi^{(2)}, J_\psi^{(3)}, J_\psi^{(4)}, J_\psi^{(5)}, J_\psi^{(6)}\}$, where A, B, and C are successively phase shifted 120 degrees with primed values representing current flowing in the opposite direction (the negative). The coil field is modelled with infinitesimal filaments that have individual currents $J_\psi^{(j)} \tau_c t_c / n_t$ (A). The coil is in a position of peak current for the B-phase (aligned with the poles). Black dashes represent continuation of the array, and blue dashes show the GMST surface for force calculation from (11).

where a typical single-sided design can be effectively air-cooled [47]. However, due to the high efficacy in providing forces this is not always problematic, as shown in a semi-active suspension application [48] (topology used for energy generation). Otherwise, this can be addressed with segmentation of the permanent magnets to allow air cooling channels and/or water cooling of the coils [43]. Being able to model 3D geometries, as later demonstrated in this article, can quantify the reduction of motor performance due to practical limitations. The other prominent practical limitation is with the radially magnetised permanent magnets that are difficult to manufacture, leading to ‘practical’ industrial designs that prefer an axial magnetisation with interlaced iron poles [47], or segmented cylindrical arc magnets with diametric magnetisation [49, 43]. Potential improvement to the force profile can be found from the inclusion of nonlinear iron segments in the stator or mover, the latter with the trade-off of introducing reluctance forces. The appropriate inclusion of iron can achieve a region of magnetisation $\approx 50\%$ higher than a permanent magnet at room temperature [50], and can be magnetised in any direction. This optimisation is not simple, or not practically possible, within the Harmonic Model using analytic methods.

There is no convincing argument that iron can improve the performance (maximise force, minimise force ripple) of the double-sided Halbach motor topology from the studies in the literature [41, 42, 51], where the authors have only shown the effects of back-iron. A brief comparison between magnet arrangements (axial-, radial-, Halbach-, magnetised) is given in [52], based upon the single-sided topology studies [53, e.g.]. Using this elemental modelling method, we can review all three magnet designs, then consider novel inclusions of iron. It can be shown that by calculating the magnetisation of the iron, sections with either no magnetisation, or a magnetisation that degrades the air-gap flux, are able to be removed. The addition

Table 1: Fixed motor parameters: M is the magnetisation of the permanent magnets with mass density D , the coil has resistivity σ and wire diameter d_t , and $\{a, r_o, \tau_a, \tau_r, \tau_c\}$ are shown in Figure 3.

M	d_t	a	r_o	$\tau_p(\tau_a + \tau_r)$	τ_c	σ^{-1}	D	
$\text{A}\cdot\text{m}^{-1}$	mm	mm	mm	mm	mm	$\Omega\cdot\text{m}$	$\text{kg}\cdot\text{m}^{-3}$	
955,000	1	1	40		18	6	1.72×10^{-8}	7500

of iron into motor designs is beneficial as the iron can more effectively route the field, i.e. flux focussing, of PMs and enhance the magnetic working point with minimal PM volume. In this article only rectangular PM and coil cross-sections are considered, with alternate trapezoidal shape selection [54] shown to have a minor influence on the results.

5. Halbach parametric study: formulation, methodology, and results

A parametric study of the axisymmetric ironless Halbach topology is performed to find a set of nondimensional motor parameters, to be used in a comparative study. A number of motor parameters are held constant, as summarised in Table 1. Primarily, the outer radius of the motor is fixed to assess the radial thickness ratios between the mover and stator, and the inner and outer magnet arrays. This study does not consider variance of the pole pitch in relation to the motor stroke. Optimal ‘secondary’ motor parameters (defined in Section 5.3) will be shown for the maximum force (Section 5.1) and minimum force ripple (Section 5.2). Then in Section 6, these ratios are used to compare motor topologies and investigate the trade-off of reducing PM volume with the addition of iron. The nondimensional ratios are summarised in Table 2 for the Halbach array, and compared to prior studies in the literature.

5.1. Maximum force

Two different figures of merit are adapted from [42] for finding an optimal maximum force. The first is a standard motor constant

$$K_M = \frac{F_z}{\sqrt{P_c}}, \quad (12)$$

with units N/ $\sqrt{\text{W}}$, that scales the axial force F_z by the copper loss in the coils P_c (or resistive power loss), that using (7) is

$$P_c = I^2 R = 2 \sum_{j=1}^3 \left(\frac{J_\varphi^{(j)} \tau_c t_c}{n_t} \right)^2 \frac{8}{d_t^2 \sigma} \sum_{k=1}^{n_t} r_t^{(k)} \quad (13)$$

with 6 coil phases and filament radii r_t . As the coil axial length τ_c and wire diameter d_t are fixed, there will always be 6 turns along the axial length per odd layer n_{t_o} , and 5 per even layer. The number of radial layers n_{t_p} is variable, giving a coil thickness t_c of $d_t + \frac{1}{2}(n_{t_p} - 1)\sqrt{3}d_t$ due to hexagonal packing. Whilst we are modelling the magnetic field as being due to filaments, for the resistance calculation we use a finite wire thickness (calculated using d_t and σ^{-1} from Table 1).

The purpose of (12) is to normalise the force by the input current and ensure that a thicker coil is not always better, given no restriction. In the same regard, it is possible to increase the force by increasing the magnet thickness. This second motor constant is adjusted to account for this

$$\kappa_M = \frac{F_z}{\sqrt{P_c M_{PM}}}, \quad (14)$$

that additionally scales F_z by the total permanent magnet mass M_{PM} , with units N/ $\sqrt{\text{W}\cdot\text{kg}}$, where

$$M_{PM} = VD = 2\tau_p \pi [t_i(2r_i + t_i) + t_o(2r_o - t_o)]D. \quad (15)$$

A thicker coil will come at the trade-off of thinner permanent magnets, and vice-versa. The first motor constant (12) will maximise the permanent magnet volume around an efficient coil, and the second (14) will additionally minimise the permanent magnet volume ('hollowing' the motor by increasing the inner radius).

The motor constants K_M and κ_M are purely geometric figures of merit, assuming fixed material properties and current density. However, they indirectly account for thermal constraints through Joule heating, as designs with higher copper losses reduce the motor constants. A complete thermal analysis (including thermal capacity, thermal derating, and PM demagnetisation) is beyond the scope of this magnetostatic optimisation study, noting thermal weightings can be applied in a post-processing stage.

5.2. Minimum force ripple and computation

The figure of merit used to quantify the force ripple is the Crest Factor (CF), applied here as

$$CF = \frac{(K_M)_{peak}}{(K_M)_{RMS}} = \frac{(F_z)_{peak}}{(F_z)_{RMS}}, \quad (16)$$

where the peak value $F_{peak} = \max(|F|)$ is scaled to the Root Mean Square (RMS). A crest factor of 1 represents a uniform force over the stroke length. There is no periodic solution in this elemental model, so to simulate this, a single wavelength of the coil ($6 \times \tau_c$) is moved ($2\tau_p$) within an array of 17 magnets axially ($9 \times \tau_a + 8 \times \tau_r$, shown in Figure 13a). The coil array is positioned $> 2\tau_p$ away from the axial ends of the magnet array in order to prevent drop-off in the magnetic flux density across the coil, and the axial force is calculated at 100 equispaced locations. At each location, the field is calculated in the air-gap on the surface specified in (11) (shown on Figure 2c) with N_ρ and N_z chosen for 120 field points per τ_c and $N_\varphi = 0$ for axisymmetry.

The crest factor in this study is calculated using idealised sinusoidal phase currents (4). This does not include dynamic effects that contribute to force ripple, such as back-EMF or inverter-induced harmonics in the coils, or eddy currents in the PMs and iron segments. This is not an inherent limitation of the model, as this complexity can be included in future work: at a point in time or motor position, the coils/filaments can be assigned an arbitrary DC current, and the PMs (including psuedo-PM iron segments) can be given an arbitrary magnetisation magnitude. The model is not contingent on all coils having idealised current waveforms or all PMs having periodically repeating magnetisation.

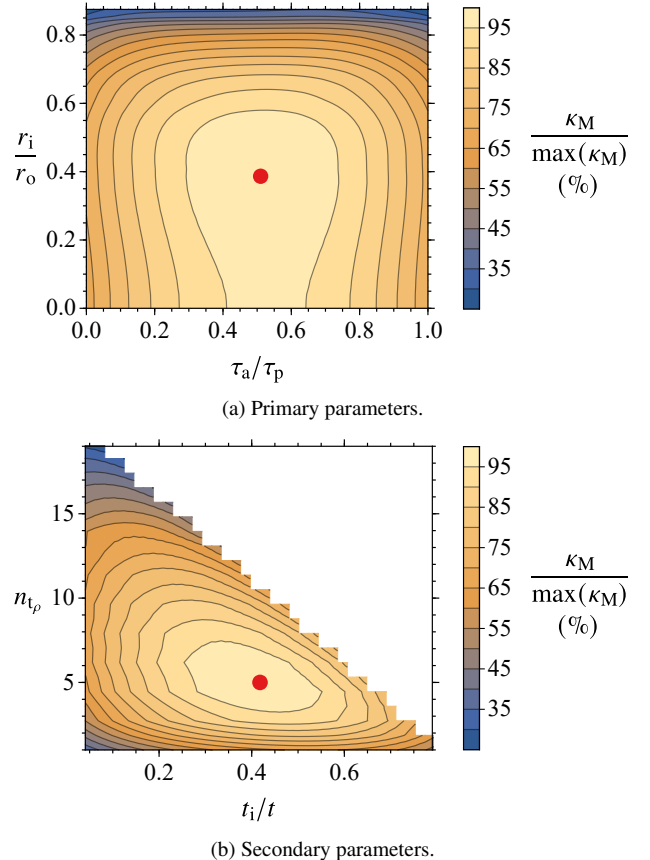


Figure 4: Parameters for maximum force in the Halbach array (Figure 3), scaled by permanent magnet mass and copper loss in (14). The optimum $\max(\kappa_M)$ is shown with ● and has a value of $24\text{N}/\sqrt{\text{W}\cdot\text{kg}}$ with parameters $\tau_a/\tau_p = 0.51$, $r_i/r_o = 0.39$, $n_{t_p} = 5$, and $t_i/t = 0.42$. (b) is unique to the optimum point on (a).

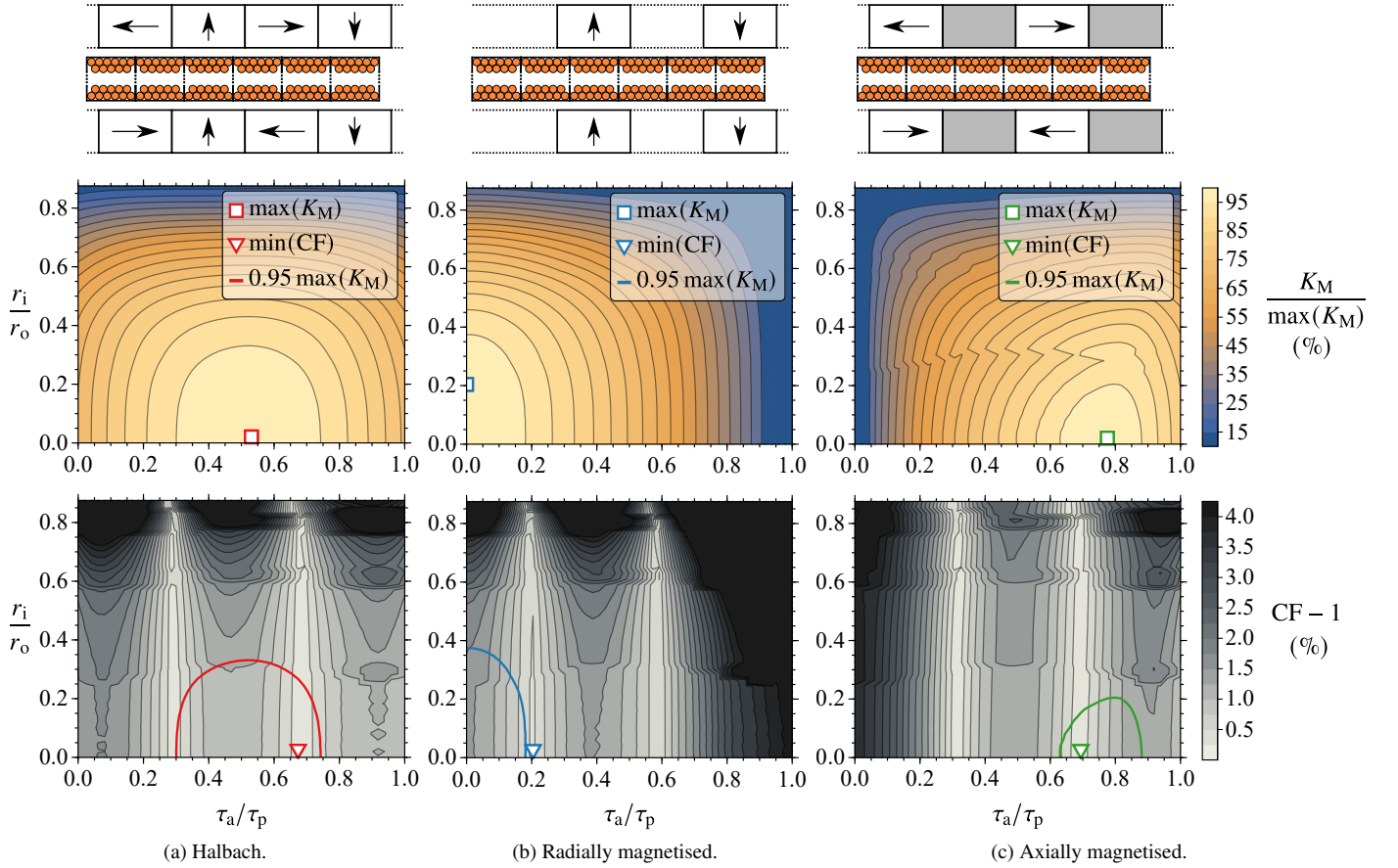


Figure 5: Three standard linear motor topologies (a-c), illustrated above plots for the motor constant (K_M , top) and crest factor (CF, bottom). The motor constant is normalised to the maximum value $\max(K_M)$ independently for each topology. Relative scales are shown in Table 3.

5.3. Nondimensional motor parameters and optimisation

Nondimensional axial and radial parameters are introduced in Figure 4 for comparison of the Halbach array at a static position in the ‘periodic’ section of the motor, at a point of peak force (as illustrated with the B-phase coil in Figure 3). Defined are two primary parameters r_i/r_o and τ_a/τ_p that scale the dominant radial and axial terms. Secondary parameters are defined as t_i/t and n_{t_p} , that scale the ratios between magnet and coil volume. For each combination of τ_a/τ_p and r_i/r_o , every sub permutation of how many n_{t_p} can fit (1, 2, 3...) is checked, along with a variable range of t_i/t ; a single sub permutation is shown in Figure 4b, relating to the point with maximum motor constant κ_M .

To find the optimal secondary parameters, a grid of 2200 primary parameters (Figure 4a) are chosen in the ranges of $0 \leq \tau_a/\tau_p \leq 1$ and $0 \leq r_i/r_o \leq 0.875$: such that the magnets (t_i and t_o) are ≥ 1 mm and the coil has at minimum 1 layer. This resulted in the simulation of 898,150 sets of motor parameters. To note, even though individual wires and magnets were modelled, no topology took more than 1 second to evaluate with vectorised MATLAB code (The MathWorks, Inc., Natick MA, USA) on a standard desktop PC (3.5 GHz processor E3-1240v5 and 16 GB RAM DDR4). This shows an advantage to initially considering the linear Halbach system, without considering the more computationally demanding nonlinearities of

the iron. Evaluation time is provided as a benchmark for the axisymmetric elemental magnetic field equations, using the same PC and publicly available code [31] in Mathematica (V12, Wolfram Research, Inc., Champaign, IL, USA): filament – 0.08 ms; axial PM – 0.95 ms; radial PM – 6.1 ms ($P = 10$). Using these figures, sequential calculation of the magnetic field at a single field point in Figure 13a is ≈ 134 ms, from 34 PMs and 6 coils with each 40 filaments each. Computation time increases by up to an order of magnitude for the equivalent non-axisymmetric geometries, detailed in [12, §6.1].

From the same dataset of Figure 4, Figure 5a shows results for the second motor constant and crest factor. The results are summarised in Table 2 and Figure 6, with comparison to three parametric studies in the literature that looked at: minimising force ripple [41, 51]; thermal effects [43, 51]; optimising motor mass [43]. Difference in the axial parameter τ_a/τ_p from all three studies can be understood using Figure 5a, where there are two regions at approximately 0.3 and 0.7 that minimise force ripple and are within 95 % of the maximum force at 0.5. This is known from classical motor theory in single-sided designs, as these ratios are generally considered to have minimised passive cogging force [2, 55]. Further, this is an intuitive result, as each coil phase has sizing $\tau_c/\tau_p = 1/3$, that matches the length of the radial or axial permanent magnets to the coil length – one coil phase can be in peak flux, and another in minimum flux,

Table 2: Optimised nondimensional Halbach parameters across various studies.

	Parameters	Reference			Figure 4	Figure 5a	
		[41]	[51]	[43]	κ_M	K_M	CF
Primary	r_i/r_o	0.175	0.32	0.31	0.39	0.02	0.02
	τ_a/τ_p	0.7	0.25	0.5	0.51	0.53	0.67
Secondary	t_i/t	0.39	0.41	0.46	0.42	0.56	0.56
	n_{t_p}	–	–	–	5	7	7

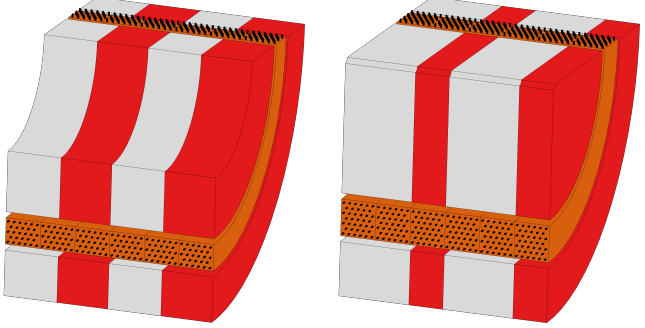


Figure 6: A to-scale quarter model 3D illustration of two periodic motor segments, showing contrasting optimal geometries dependent on optimisation parameter.

aligning geometry to the phases.

The radial parameter r_i/r_o has negligible effect on force ripple, and largely depends upon the choice of motor constant. When scaling for permanent magnet volume, the optimal design will be a hollow motor, due to the aforementioned radial asymmetries. However, there is a significantly large region $r_i/r_o = 0 \rightarrow 0.3$ that is within 95 % of the maximum of both motor constants κ_M and K_M , explaining the variation here between studies. Using an optimisation similar to [43] with κ_M , a similar result to the Harmonic Model is attained with this Elemental Modelling Method. Finally, the ratio between the coil and magnet volumes (based on t_i/t) were similar in all studies, except for the almost-solid motor found with K_M . This motor topology has a range of variability possible in the design to maximise force and/or minimise force ripple, without significant detriment. Dynamic effects are not considered here, which are predicted to restrict this parameter range further.

6. Comparative study of motor topologies with iron

In this section we investigate whether alternate motor topologies can outperform the Halbach topology (Figure 3). A general comparative study is shown in Figure 5 with radial and axial magnetisations, using the optimal secondary parameters from Section 5.3; only K_M is presented with variance of the primary parameters τ_a/τ_p and r_i/r_o . The purpose of analysing the traditional topologies is to attain optimal geometries to strategically place iron into, towards improving both the motor constant and crest factor. The optimal geometries for each topology, and both design goals, are shown in Table 3.

Table 3: Summary of the optimal points from Figure 5, where all have common secondary parameters of $n_{t_p} = 7$ and $t_i/t = 0.56$. The Crest Factor (CF) is normalised to a percentage difference.

Topology	Maximum K_M (N/ \sqrt{W})				Minimum CF			
	K_M	CF – 1	$\frac{\tau_a}{\tau_p}$	$\frac{r_i}{r_o}$	K_M	CF – 1	$\frac{\tau_a}{\tau_p}$	$\frac{r_i}{r_o}$
Halbach	25.9	0.87 %	0.53	0.02	25.4	0.09 %	0.67	0.02
Radial	18.0	1.30 %	0.00	0.20	16.9	0.20 %	0.20	0.02
Axial	23.6	0.71 %	0.78	0.02	23.3	0.07 %	0.69	0.02

For the Halbach and axial topologies, the normalised crest factor can be reduced by an order of magnitude when shifted from the point of maximum motor constant. This significant benefit comes with a minor trade-off of 2 % of K_M for the Halbach topology and 1.3 % of K_M for the axial topology. The geometries chosen for iron augmentation have the minimum crest factor, chosen towards a goal of eliminating force ripple in the magnetostatic design. For the radially magnetised array ($\geq 0.95\max(K_M)$) require a low τ_a/τ_p , thus are unlikely see an improvement in radial flux from adding iron as the optimal topologies for the axially magnetised array require a high τ_a/τ_p . The axial permanent magnets are the most important part of the tubular linear motor.

To incorporate iron into the model with the axially magnetised array (and in the following section), we explicitly follow the methodology presented in Section 2. Each cylindrical iron piece is discretised into $64(8 \times 8)$ equivalent permanent magnets, with equally-sized cross-sectional segments, chosen as this has been shown to have good agreement with FEA for the air-gap flux, whilst remaining computationally feasible for this large study [20]. The convergence tolerance for the iron iteration was chosen at ± 1000 A/m and the iron is modelled using the nonlinear single-line equivalent B - H - μ_r curves [21, §A], based upon the soft magnetic composite Somaloy-1000-3P [56]. Whilst it is possible to compare different iron compounds with this modelling methodology, this is out of the scope of the current work.

6.1. Iron augmentation

Theoretically, it should be possible to add iron into a design and see an improvement in the air gap flux, as traditionally seen with back-iron. The question is: when working within a fixed size constraint, is the trade-off from permanent magnet volume to iron going to yield an improvement to the force and/or force ripple? To demonstrate the capability of the modelling approach we look at some simple augmentations to the Halbach array, shown in Figure 7a to 7h. The addition of iron improves the translational force and reduced the force ripple in Figure 7j (radial) and 7k (axial); however, the iron does not improve both figures of merit for the Halbach array in Figure 7l, with the best variant having an inner iron core, reducing the thickness of the inner permanent magnets by 20 % with minimal trade-off to the translational force and force ripple.

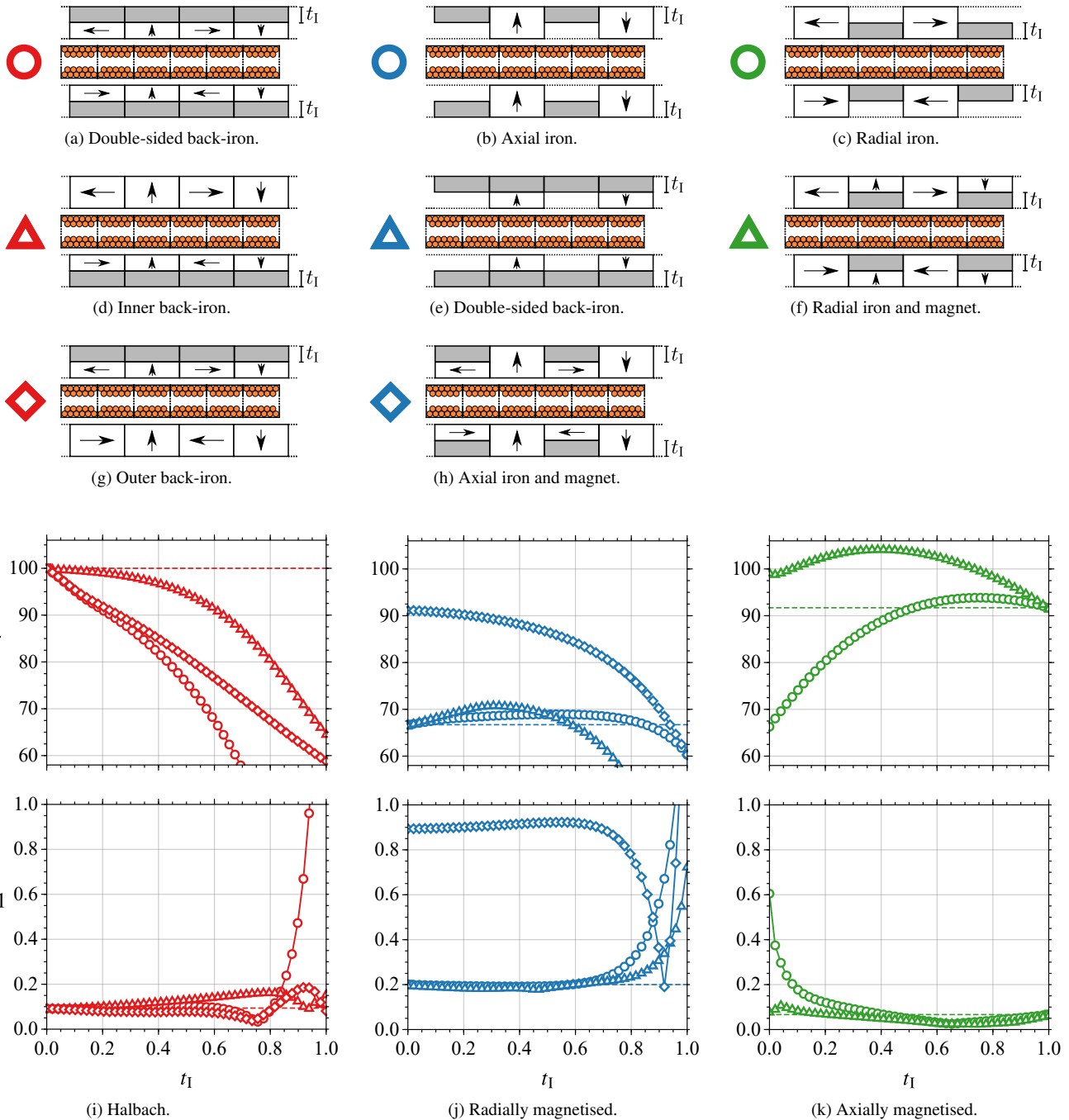
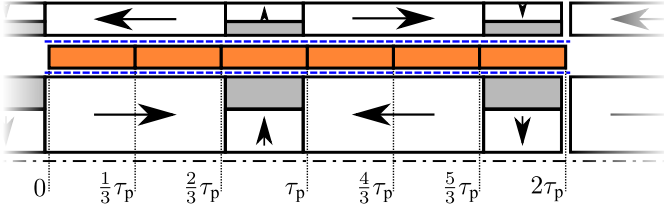


Figure 7: Altering the standard motor topologies from Figure 5 with the iron augmentations of (a)-(h), then comparing the figures of merit in (i)-(k). The motor parameters are chosen using Table 3, optimised for a minimum crest factor, and unique for the designs of (i) Halbach, (j) radial, and (k) axial. An iron thickness parameter is introduced such that $t_I = 0$ has no iron, and as t_I increases, it reduces the permanent magnet volume (if present). The motor constant reference value is the same for all topologies ($\max(K_M) = 25.4 \text{ N}/\sqrt{\text{W}}$), thus all plots can be compared left to right. The horizontal dashed line in each plot is a reference line for the changes to each topology: the force (top plots) has improved if above the line, and the force ripple (bottom plots) has improved if below the line.

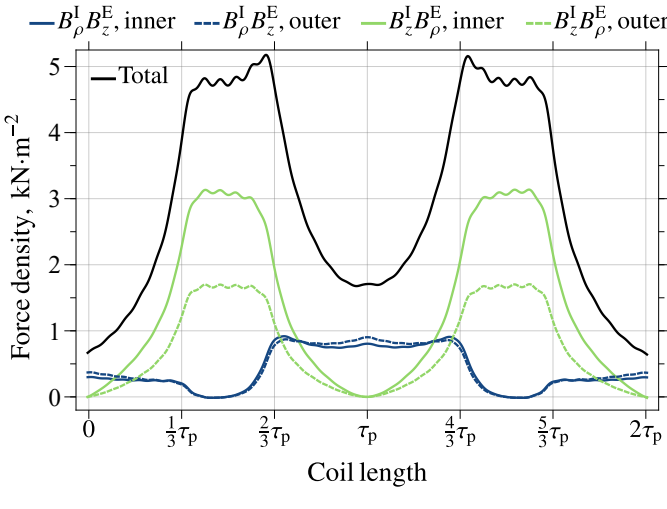
The addition of radial permanent magnets to the axially magnetised array in Figure 7k increases the translational force and reduces the force ripple, up until the iron has reduced in thickness by 60 %. In part, this can be explained by the second topology in Figure 7c; removing the iron furthest from the coil (close to r_i and r_o) actually improves both the motor constant and crest factor. Significantly, with $t_I = 0.39$ and the radial per-

manent magnet, this design outperforms the Halbach topology (Table 3) within our design constraints with relative changes of 104 % K_M (or $26.4 \text{ N}/\sqrt{\text{W}}$) and 56 % ($CF - 1$) (or 0.05 %). This also has the added benefit of reducing material cost, due to the reduction of permanent magnet volume.

For the optimal topology found in this comparative study, Figure 8 shows components of the analytic air-gap magnetic



(a) Motor topology with reference for coil length in (b) and Figure 9.



(b) Force density components.

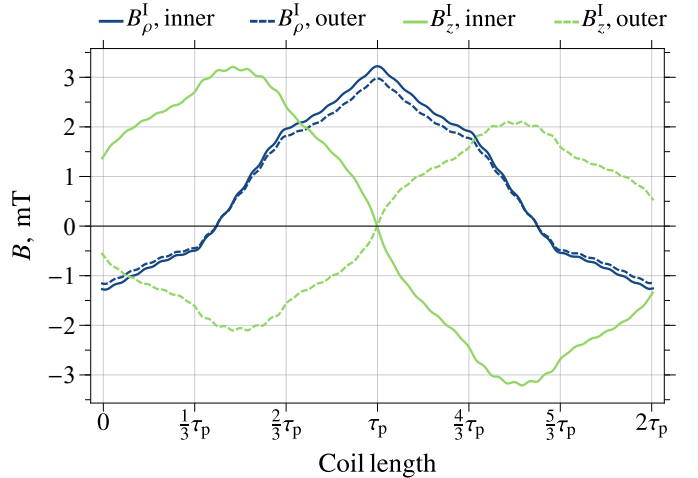
Figure 8: The force densities along two lines (inner, outer) in the air-gap, 0.1 mm away from the coil on either side, shown by the blue dashed lines in (a). Components of the magnetic flux density along these two lines, used to calculate the force density, are shown in Figure 9. The motor topology and dimensions are selected from Table 3 and Figure 7f, with $\tau_a/\tau_p = 0.69$, $r_i/r_o = 0.02$, and $t_l = 0.39$. The current in each coil filament per phase is $\{A, C', B, A', C, B'\} = \{0.5, -0.5, -1, -0.5, 0.5, 1\}A$, for total force of 17.41 N.

flux density, for a single coil wavelength (6 phases, $2\tau_p$) within a long stator. To understand how the fields produce force, we return to (11)

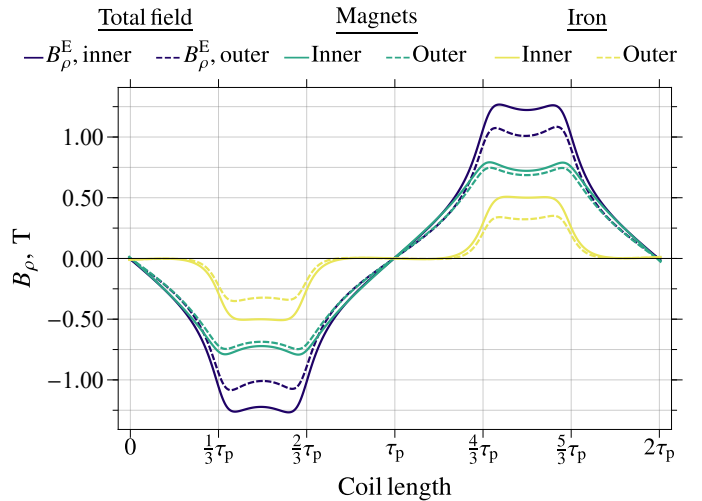
$$\frac{F_z}{2\pi r_z^*(z_2^* - z_1^*)} \approx \mu_0^{-1} \sum_{s=1}^2 (-1)^s (B_\rho^E B_z^I + B_z^E B_\rho^I) \Big|_{r_s^*}, \quad (17)$$

where $s = 1$ is the inner surface and $s = 2$ the outer. The force density in (17) is the shear components of the Generalised Maxwell Stress Tensor (cylindrical shell surface) that contributes 91 % of the total force in this case study, with the final contribution from the pressure components (annulus surfaces) not shown. This is a 2D axisymmetric mesh, with the 3D analogue visualised later in Figure 10d. The pressure components are typically ignored in the periodic Harmonic model using the classical Maxwell Stress Tensor, yet this non-negligible coil end effect is captured in our study using the elemental model.

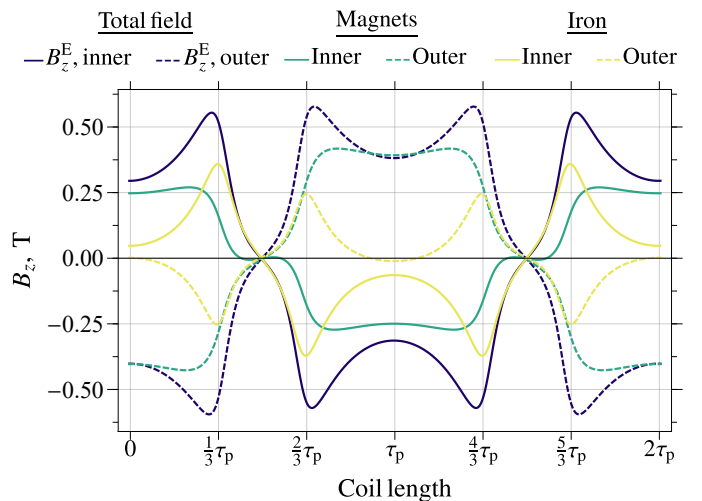
An advantage of using this modelling method over numeric solvers such as FEA, is being able to quantify and understand the contribution from each component in a single nonlinear model. The iron poles contribute 28 % of the total force, whilst being 13 % of the total permanent magnet mass (per τ_p). The radial magnetic flux density from the iron in Figure 9b is fo-



(a) Internal field components – coils only.



(b) Radial external field components.



(c) Axial external field components.

Figure 9: Components of the air-gap magnetic flux density used to calculate the force density in Figure 8: (a) coil array in mover, (b,c) permanent magnets and iron in the stator.

cused over one coil phase, at the position of peak current in each phase, and the axial magnetic flux density from the iron in Figure 9c creates symmetry in the total axial flux B_z^E across the inner and outer surfaces. This matches to the coil profiles in Figure 9a that have (approximately) equivalent radial flux B_ρ^I , for the force density $\mu_0^{-1} B_z^E B_\rho^I$. The solenoidal nature of the coil gives a higher axial flux B_z^I on the inner surface, hence the thickness proportions of the inner and outer magnet-iron arrays are balanced to match that with B_z^E for the second force density component $\mu_0^{-1} B_z^I B_\rho^E$. Small ripples in the coil field are observed due to the modelling of discrete filaments (turns) in the array. Whilst the field from the coil is very small relative to the permanent magnets and iron, these ripples are pronounced in the force density (Figure 8b). For a coil with a low number of turns, as in this case study, consideration of these higher order harmonics can lead to a more precise optimisation.

6.2. 3D diametric arc transformation and summary

The theme of the results thus far has been to find a motor topology that can outperform the standard double-sided Halbach array. In Section 5 a set of optimal secondary parameters were found for all permutations of the Halbach array that defined the radial thickness ratios of the coil and inner/outer magnet arrays. In that section, those parameters were used in each topology of the comparative study (Halbach, radial, axial), analysed in terms of the primary parameters of motor thickness ($r_o - r_i$) and pole-pitch ratio. Using only one set of these parameters for each topology (a geometry with the minimum crest factor), a number of iron augmentations were made to find improvements in both the motor constant and crest factor. What is highlighted is a significant constraint of all possible permutations, based upon optimal constraints for the canonical Halbach array. When it comes to transforming this model into 3D, this again opens up a number of interesting variations that are out of the scope of demonstrating this modelling method. These variations include varying the axial and radial spacing of the permanent magnets, randomising the permanent magnet magnetisations, considering non-axisymmetric magnetisations of the iron and/or permanent magnets, etc.

The most topical 3D transformation in the literature [49] is conversion of radially magnetised permanent magnets to diametrically magnetised arcs, e.g. Figure 10a. Typical analyses in the literature have not been completed with a true 3D model using analytic methods, only 2D approximations with no azimuthal spacing, e.g. Figure 10b. The Halbach array has a large range of parameters that are within 95 % of the peak force in the axisymmetric case (Figure 5a); however, shown in Figure 11 is significant sensitivity in these results when considering a more ‘real-world’ model. When there is no azimuthal spacing between the diametric permanent magnets and as the number of segments increases, the result will trend towards the axisymmetric case, or radially magnetised permanent magnet ring. The segmentation results for this $\theta = 0$ case match those in [49] for 1, 3, and 5 % reductions.

When fabricating linear motors, there are tolerances between the magnets and non-magnetic support structures (glue, casing),

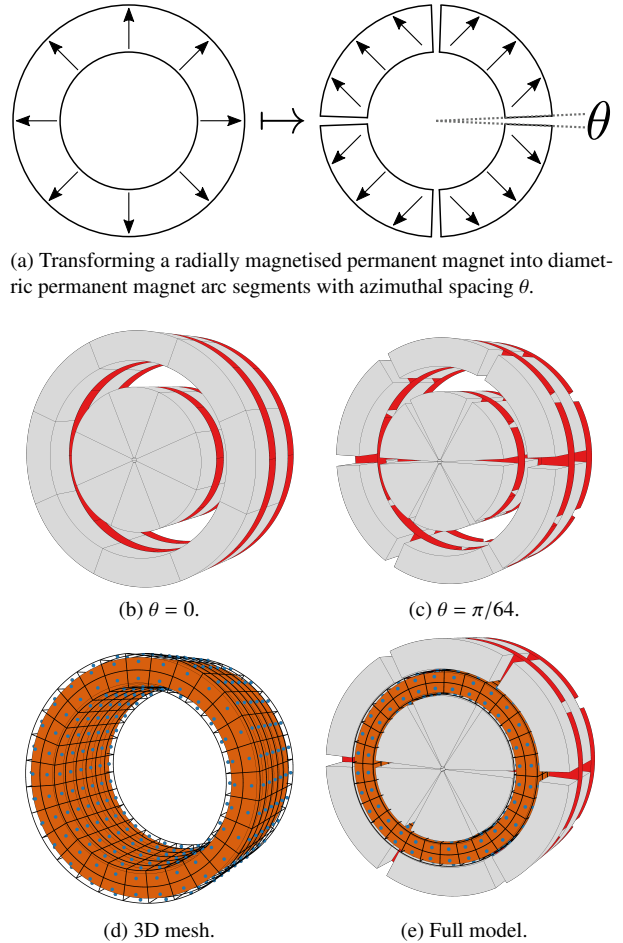


Figure 10: The diametric (red) and axial (gray) permanent magnets are skewed by $\pi/\text{segments}$ – half the azimuthal period, as shown in (b,c). A 3D discretisation of the analytic field is now required in (d,e) due to (a), relative to the axisymmetric mesh shown in Figure 1 Step 6.

the so-called stacking factor that increases with increasing use of components. In this regard, it is useful to also offset the azimuthal angles of the permanent magnets along the length of the motor, as shown in Figure 10c with the multi-colours. With these spacings and rotations, the motor constant significantly drops off with higher segmentation, although the crest factor will always improve with higher segmentation. With $\theta = \pi/256$ ($\approx 0.7^\circ$) and 8 azimuthal segments, the motor constant is reduced by 4 % and crest factor increased by 2.4 %, respectively.

6.3. Finite Element Analysis comparisons

Optimal nondimensional parameters for the Halbach topology were found in Section 5.3 using the Elemental Modelling Method, and are consistent with comparable studies in the literature that used the Harmonic Model. For a complete verification of the results, detailed comparisons with FEA are shown for an optimal topology: the non-periodic spatial magnetic flux density (Figure 12) and the force profile during a motor stroke inclusive of end effects (Figure 13).

It is expected that analytic solutions from the elemental model match identically with FEA, assuming the models are equivalent. This is the case for the permanent magnet field solutions

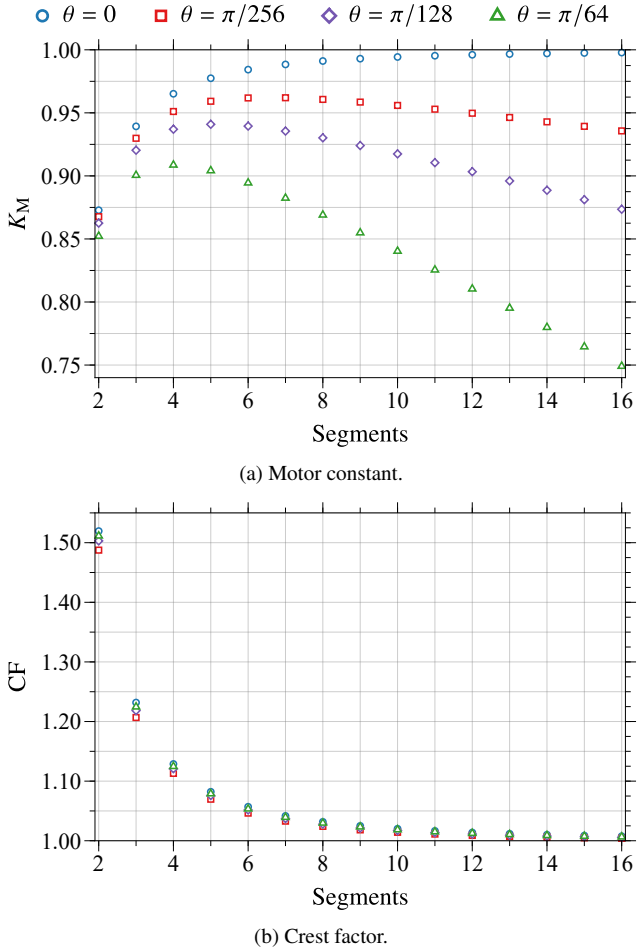


Figure 11: Reduction in the (a) force and increase in the (b) force ripple when varying the number of diametrically magnetised arcs, normalised to the optimal axisymmetric radial permanent magnet (Figure 10a). Motor dimensions are selected from Table 3 for the Halbach array with $\tau_a/\tau_p = 0.67$ and $r_i/r_o = 0.02$.

used in this article with $\mu_0 = 1$ [12]; however, there are caveats for the semi-analytic force calculation regarding both the physical interpretation of coil current density and linearisation of the iron. Further, we have not yet considered variable permeability of the permanent magnets with $\mu_r \neq 1$. The FEA model has a block coil (Figure 2), not filaments, and interpolation methods for the B - H curve between the analytic code and FEA software differ slightly. Regardless, in this section we observe differences of $<0.5\%$ across all examples comparing the force from the semi-analytic model and FEA with: non-periodic sections of (short) Halbach and iron-augmented Halbach topologies (spatial field Figure 12); a Halbach array with non-unity relative permeability (Figure 14); and, axial translation of the coil through a long Halbach array (force profile, Figure 13). The flux density levels in the fields should be equivalent between models with slight variance in distribution, thus when we are integrating the ‘spatial average’ will be similar.

All FEA results were found using Maxwell 2D, within the ANSYS Electronics Desktop 2022 R2 (ANSYS, Inc., Canonsburg, PA, USA). The software has ‘adaptive meshing’ that subdivides adjacent elements in each mesh refinement with the es-

timated highest energy error. The simulations were run until an energy error and delta energy of $<0.0001\%$ was met. The total energy error is the ratio of the divergence ($\nabla \cdot \mathbf{B}$) to the total energy in the model, and the delta energy is the difference between the total energy in each successive mesh refinement. Each model/position takes a few minutes on a standard PC.

A non-periodic section of both the optimal Halbach and augmented-Halbach topologies is shown in Figure 12. The force on both coils is approximately equal as one of the iron poles is significantly demagnetised. This can be visually seen with the air-gap field being similar magnitude and shape, although the highlight is the significant improvement in magnetic flux density through the iron pole versus the radial permanent magnet. This is shown in Figure 14a, with the iron effectively achieving magnetisations in excess of $1.5 \text{ MA}\cdot\text{m}^{-1}$ versus the permanent magnets with $0.955 \text{ MA}\cdot\text{m}^{-1}$, i.e. $\approx 50\%$ higher. The magnetic field through these iron poles does somewhat vary from that in the FEA model; however, this does not affect the air-gap flux where the force is calculated. We could increase the iron discretisation in order to reduce the internal field differential to FEA, yet this would introduce an unnecessary computational increase. One benefit of this analytic linearisation of the iron is that we can coarsely discretise the iron and still accurately model the magnetisation, and hence field, with a low computational burden. Outside of this iron region, there appears to be a pattern in the ‘numerical noise’ of the analytic magnetic field results compared to FEA. This is due to a finite series solution for the radially magnetised permanent magnet, where we have chosen a low number of terms in favour of rapid computational speeds – this is inconsequential to the results, yet will appear when looking at such low magnitudes [12, §3.5, $z = \frac{1}{2}$].

An extension to the linearisation of the highly nonlinear iron poles is varying the relative permeability of the permanent magnets. Each permanent magnet in Figure 14c is discretised into an 8×8 grid, similar to the iron poles. The superimposed permanent magnets are assumed isotropic, although this can also be weighted relative to the easy axis e.g. $M_z = 0$ or $M_\rho = 0$. Comparing the force result to Figure 12a, with a constant relative permeability of $\mu_r = 1.1$, the force increases by 6.4 %. In addition to transforming the model into a 3D design, as shown in Section 6.2, including nonlinearity in the permanent magnets also introduces significant change to the optimal linear and axisymmetric 2D results.

The force profile, including all radial and axial end effects is shown in Figure 13 and compared to FEA. This figure provides context as to what a small crest factor looks like, and it also shows how the force profile is never truly periodic, as due to superposition the axial end effects are always propagated into the results. As mentioned previously, we do not expect the analytic and FEA models to be identical due to minor differences in the coil, and both results are within $\approx 0.5\%$ respectively. A significant argument towards the benefit of analytic solutions is shown here, where fidelity to capturing the minor force ripple is completely lost in the FEA solution. Further, there is no demonstration of symmetry about the midpoint of the array and otherwise the solution appears within a noise floor.

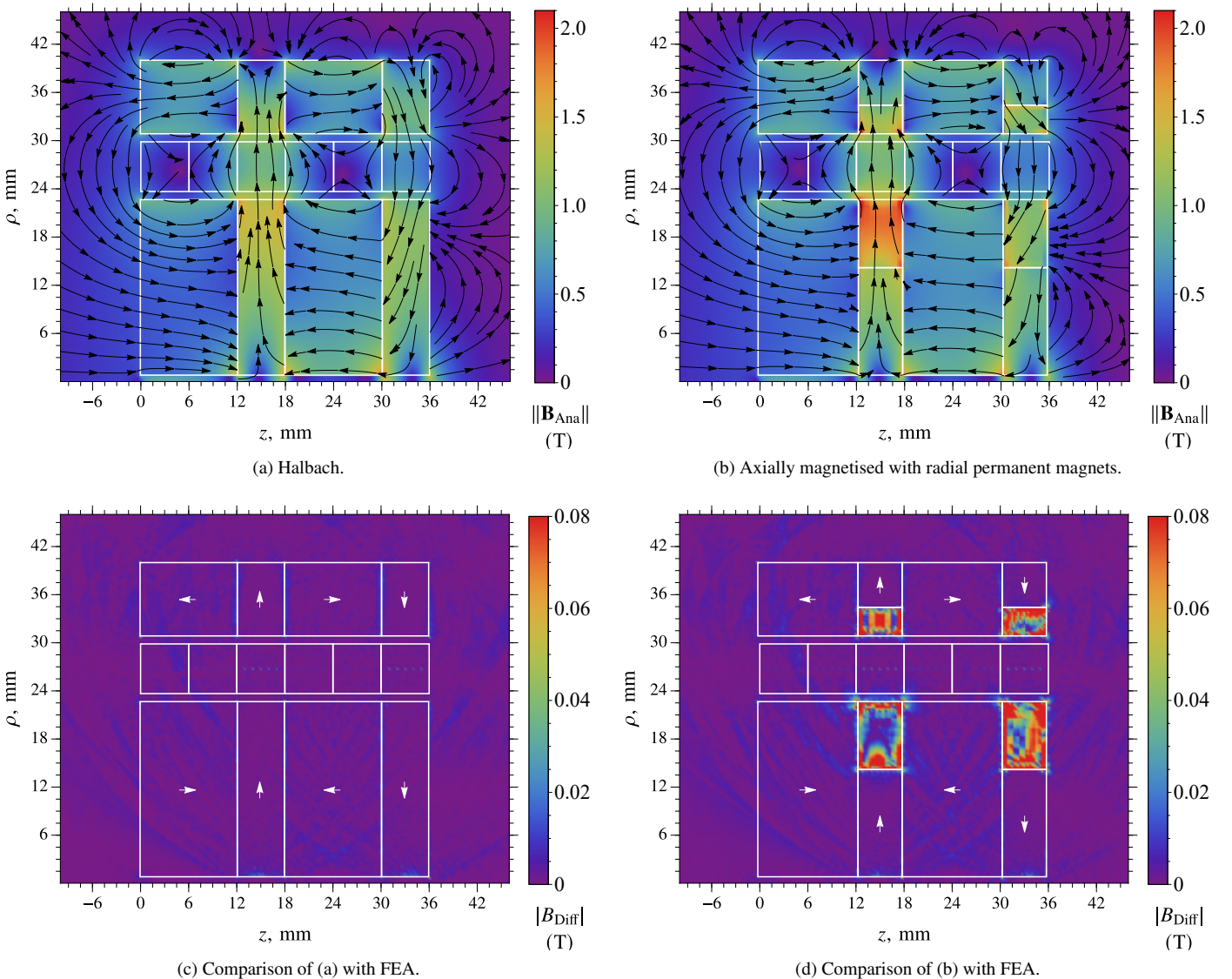


Figure 12: A section, or singular wavelength, of the optimal Halbach and axially magnetised motor topologies (Figure 5) for minimum CF, with geometries from Table 3. The axially magnetised motor is augmented with radial permanent magnets (Figure 7f) with $t_1 = 0.39$. In (a) and (b) are the axisymmetric analytic magnetic fields, the superposition from all permanent magnets and coil filaments in the elemental model. The difference in the magnetic flux density from (a) and (b) compared to FEA ($B_{\text{diff}} = \|\mathbf{B}_{\text{Anal}}\| - \|\mathbf{B}_{\text{FEA}}\|$) is shown in (c) and (d). The force on the coil filaments is 14.309 N in (a) and 14.169 N in (b), compared to the FEA results with block coils of 14.240 N (a) and 14.124 N (b) – differences of 0.48 % and 0.32 %, respectively.

6.4. Discussion on computational efficiency

Analytic magnetic field solutions for each element in the model solve precisely and quickly, as discussed in Section 5.3 and shown in [12]. That being said, the computational efficiency of a particular motor design using the Elemental Modelling Method is completely dependent upon the number of elements (PMs, coils) in the model, due to the superposition of field solutions, and on the number of field points required to calculate the force (dependent on the method used in Section 3). A large number of magnetic sources in a model will invariably come at computational expense — this is the benefit of the distributed-parameter Harmonic Model, which achieves efficiency by introducing additional assumptions on boundary conditions, permeability, geometry, and symmetry, often at the

cost of physical accuracy. Transitioning to the 3D model in Section 6.2 multiplies the computation time by the number of azimuthal segments, in addition to requiring significantly more mesh points.

Computation times for a number of case studies using the semi-analytic application of the block model (3), filament model (5), and GMST (8) are shown in [21], and compared to equivalent FEA simulations in both 2D and 3D models. Without optimised code for the magnetic field solutions (e.g., exploiting parallel computing techniques), the analytic-based methodology can be orders of magnitude faster than FEA (a highly optimised software package) at computing the force and torque, depending on the required solution precision, due to linear scaling with the number of field point computations. However, the lin-

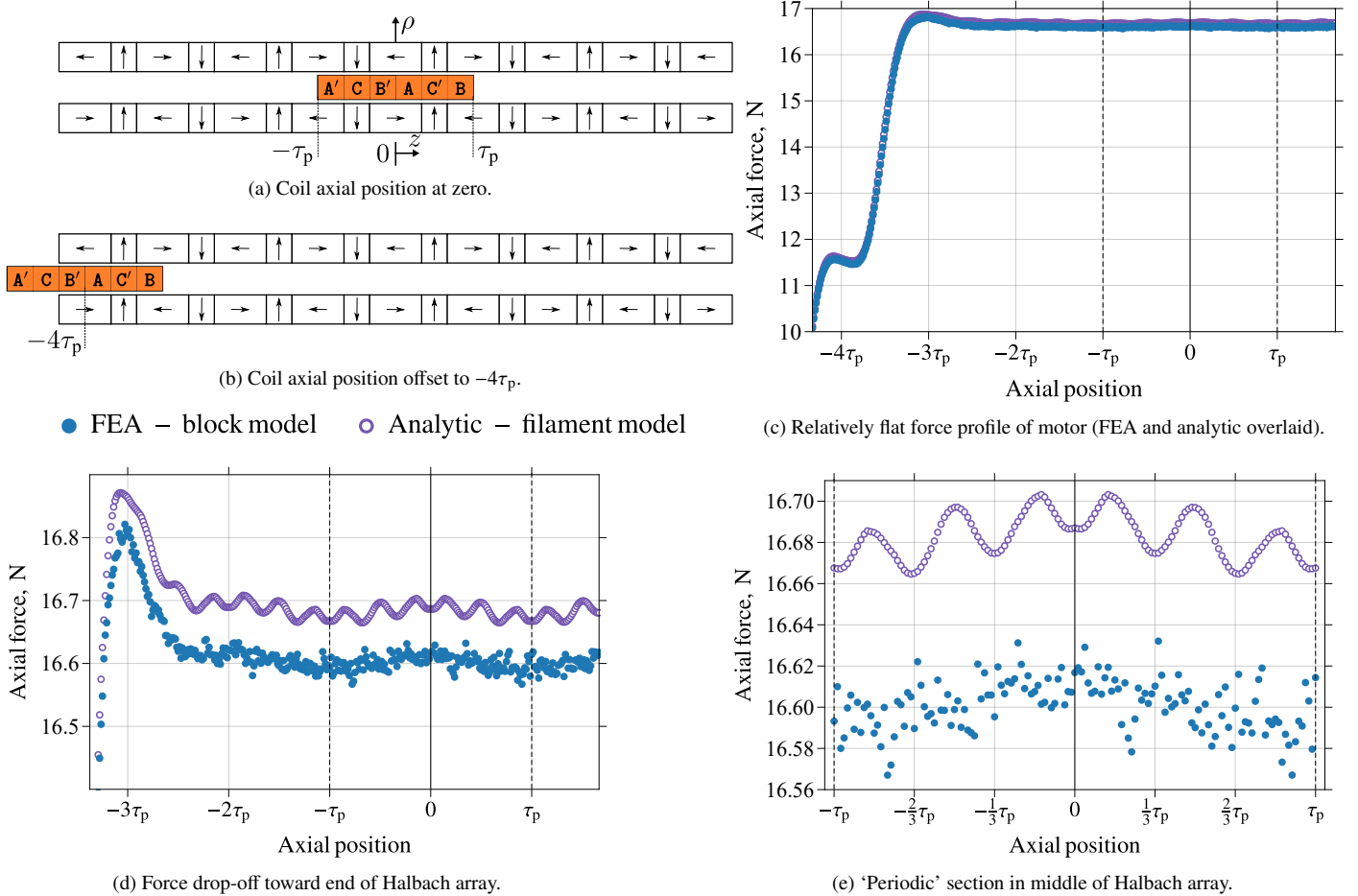
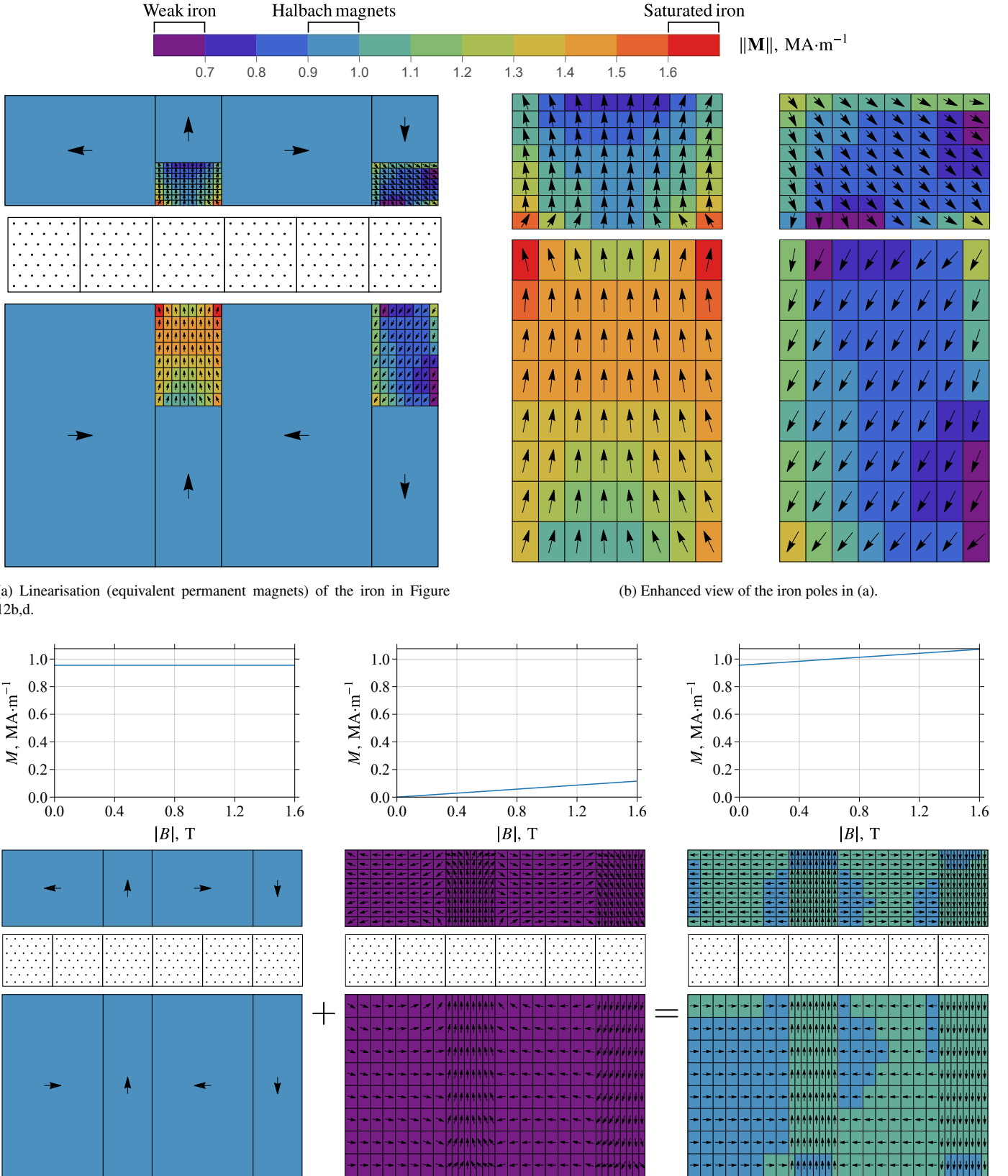


Figure 13: The motor force profile from a model using coil filaments and analytic magnetic field solutions, compared to an FEA model with solid/block coils (reference Figure 2). Each coil filament has a peak current of 1 A, that is equivalent to a block current density of $\hat{J}_\varphi = 1.049 \text{ MA}\cdot\text{m}^{-2}$ in FEA. Translation of the coil through the Halbach array is illustrated, not to scale, in (a) and (b). Motor dimensions are selected from Table 3 with $\tau_a/\tau_p = 0.67$ and $r_i/r_o = 0.02$. For the ‘periodic’ section of coil translation in (e) marked with vertical dashed lines, the analytic force has an RMS of 16.683 N, with FEA at 16.601 N – a difference of 0.49 %.

earisation process of the iron (into an equivalent set of PMs) has an exponential computational expense: the field from each iron segment needs to be calculated at every other iron segment. If significant discretisation of the iron regions is required, then the linearisation process can quickly become computationally expensive relative to FEA. For the purpose of a parametric study, it has been shown that a coarse discretisation of typical iron regions in a linear motor is often sufficient due to the iron segments having large regions of uniform magnetisation [20, 21]. A detailed analysis of the computational efficiency of the linearisation process, and potential improvements, remains a topic for future work. Irrespective of computation time, analytic solutions are able to highlight unique phenomena that are lost in the numerical precision of FEA, as shown in Figure 13e.

Beyond analysing the computational efficiency between analytic models and FEA for a single motor position, an advan-

tage of developing the Elemental Modelling Method is for dynamic studies with multiple mover/rotor positions and various operational frequencies. Memoisation techniques can be used to avoid repeated computation, as the analytic magnetic field equations are scaled by a constant-magnitude current density or magnetisation, and the airgap surface on which the field is evaluated can be chosen arbitrarily. For example, the GMST surface in Figure 3 can remain in a constant relative position to the coil array as it moves. Thus, the magnetic field from each coil filament only needs to be calculated once for each mesh point, with the stored result scaled by an arbitrary current density to give the magnetostatic result at any time point. A similar process can be used for the PM fields, precomputing the magnetic field along the entire path of the coil. Further computational improvement can also be realised by implementing the field solutions in a compiled language (such as C) instead of an interpreted one.



7. Conclusion

Implementation of the Elemental Modelling Method is demonstrated in this article with a case study on a tubular double-sided Halbach permanent magnet motor with a slotless mover. The model can include all end effects when using axisymmetric-2D or 3D analytic magnetic field solutions, and it is demonstrated how to include nonlinear permeabilities from iron or permanent magnets – detail not possible in traditional Harmonic Models. The utility of this new method is shown with a parametric study that found an optimal set of nondimensional parameters for the Halbach topology, before performing a comparative study with radial and axial magnetised topologies, assessing novel changes to the arrays. A hybrid design is proposed that adds iron poles to the Halbach array, giving the motor both a higher force capability and lower force ripple than the optimal ironless Halbach array. The study maintained a primary constraint of fixed total motor volume, where introduction of iron typically came with reduction in the permanent magnet volume/mass, leading to conventional back-iron being inefficient for the inherently self-shielding Halbach array. While some of the investigated designs may not be optimal within performance figures of merit, these designs may offer ease in manufacturability and the analysis is informative for the development of cost functions that aim to reduce the permanent magnet volume.

Results of the parametric and comparative studies were verified with FEA models, with the force differential being less than 0.5 %, respectively, on all variants: a topology without iron (linear), a topology with iron and nonlinear relative permeability, and a topology including permanent magnets with a linear relative permeability. These results are observed over the full axial force profile of the motor, including regions of (approximate) periodicity and overhung regions where the mover is heavily affected by end effects. The optimal topology found has a crest factor close to one, yet still has force ripple characteristics due to the discrete coil phases and the modelling of individual coil wires in each. This fidelity is not captured within a converged FEA solution due to its numerical noise floor, highlighting the accuracy and computation efficiency of this analytic modelling method for linear or rotary motors.

Acknowledgements

This work was supported in part by the Advanced Electromagnetics Group; in part by the Australian Government Research Training Program Scholarship; and in part by the Faculty of SET, University of Adelaide.

References

- [1] D. Trumper, W.-J. Kim, M. Williams, Design and analysis framework for linear permanent-magnet machines, *IEEE Transactions on Industry Applications* 32 (2) (1996) 371–379.
- [2] J. Wang, G. Jewell, D. Howe, A general framework for the analysis and design of tubular linear permanent magnet machines, *IEEE Transactions on Magnetics* 35 (3) (1999) 1986–2000.
- [3] B. Gysen, K. Meessen, J. Paulides, E. Lomonova, General formulation of the electromagnetic field distribution in machines and devices using Fourier analysis., *IEEE Transactions on Magnetics* 46 (1) (2010).
- [4] J. Wang, D. Howe, G. Jewell, Fringing in tubular permanent-magnet machines: Part I. magnetic field distribution, flux linkage, and thrust force, *IEEE Transactions on Magnetics* 39 (6) (2003) 3507–3516.
- [5] P. M. Morse, H. Feshbach, Methods of theoretical physics, Vol. 1 & 2 of International series in pure and applied physics, McGraw-Hill, New York, 1953.
- [6] G. L. Cain, G. H. Meyer, Separation of variables for partial differential equations: an eigenfunction approach, Studies in advanced mathematics, Chapman & Hall/CRC, Florida, 2005.
- [7] E. P. Furlani, Permanent Magnet and Electromechanical Devices: Materials, Analysis, and Applications, Electromagnetism, Elsevier Science, 2001.
- [8] J. L. O'Connell, W. S. Robertson, B. S. Cazzolato, Simplified equations for the magnetic field due to an arbitrarily-shaped polyhedral permanent magnet, *Journal of Magnetism and Magnetic Materials* 510 (2020) 166894.
- [9] C. Rubeck, J.-P. Yonnet, H. Allag, B. Delinchant, O. Chadebec, Analytical calculation of magnet systems: Magnetic field created by charged triangles and polyhedra, *IEEE Transactions on Magnetics* 49 (1) (2013) 144–147.
- [10] J. Janssen, J. Paulides, E. Lomonova, 3D analytical field calculation using triangular magnet segments applied to a skewed linear permanent magnet actuator, *COMPEL* 29 (4) (2010) 984–993.
- [11] R. Ravaud, G. Lemarquand, Magnetic field produced by a parallelepipedic magnet of various and uniform polarization, *Progress in Electromagnetics Research* 98 (2009) 207–219.
- [12] M. Forbes, W. S. P. Robertson, A. C. Zander, J. J. H. Zander, Anthony C. and Paulides, The magnetic field from cylindrical arc coils and magnets: A compendium with new analytic solutions for radial magnetization and azimuthal current, *Advanced Physics Research* 3 (7) (2024) 2300136.
- [13] F. Reich, O. Stahn, W. Müller, The magnetic field of a permanent hollow cylindrical magnet, *Continuum Mechanics and Thermodynamics* 28 (5) (2016) 1435–1444.
- [14] A. Caciagli, R. J. Baars, A. P. Philipse, B. W. Kuipers, Exact expression for the magnetic field of a finite cylinder with arbitrary uniform magnetization, *Journal of Magnetism and Magnetic Materials* 456 (2018) 423–432.
- [15] F. Slanovc, M. Ortner, M. Moridi, C. Abert, D. Suess, Full analytical solution for the magnetic field of uniformly magnetized cylinder tiles, *Journal of Magnetism and Magnetic Materials* 559 (2022) 169482.
- [16] F. Masiero, E. Sinibaldi, Exact and computationally robust solutions for cylindrical magnets systems with programmable magnetization, *Advanced Science* 10 (2301033) (Jul. 2023).
- [17] C. Snow, Magnetic fields of cylindrical coils and annular coils., no. ii, 29 p. in National Bureau of Standards applied mathematics series ;38, U.S. Govt. Print. Off., Washington, 1953.
- [18] L. Urankar, Vector potential and magnetic field of current-carrying finite arc segment in analytical form, part I: Filament approximation, *IEEE Transactions on Magnetics* 16 (5) (1980) 1283–1288.
- [19] J. Conway, Exact solutions for the magnetic fields of axisymmetric solenoids and current distributions, *IEEE Transactions on Magnetics* 37 (4) (2001) 2977–2988.
- [20] M. Forbes, W. S. P. Robertson, A. C. Zander, J. J. H. Paulides, Boundary-free analytic magnetic field calculations including soft iron and permanent magnets using an iterative discretization technique, *IEEE Transactions on Magnetics* 57 (2) (2021) 1–5.
- [21] M. Forbes, W. S. P. Robertson, A. C. Zander, J. Vidler, J. J. H. Paulides, A generalised Maxwell stress tensor for semi-analytic force and torque between permanent magnets, coils, and soft iron, *Applied Mathematical Modelling* 144 (2025) 116050.
- [22] R. L. J. Sprangers, J. J. H. Paulides, B. L. J. Gysen, E. A. Lomonova, Magnetic saturation in semi-analytical harmonic modeling for electric machine analysis, *IEEE Transactions on Magnetics* 52 (2) (2016) 1–10.
- [23] J. Bao, B. L. J. Gysen, E. A. Lomonova, Hybrid analytical modeling of saturated linear and rotary electrical machines: Integration of fourier modeling and magnetic equivalent circuits, *IEEE Transactions on Magnetics* 54 (11) (2018) 1–5.

- [24] A. Mollaeian, A. Kundu, M. S. Toulabi, M. U. Thamm, S. Kim, J. Tjong, N. C. Kar, Fourier-based modeling of an induction machine considering the finite permeability and nonlinear magnetic properties, *IEEE Transactions on Energy Conversion* 36 (4) (2021) 3427–3437. doi:10.1109/TEC.2021.3085748.
- [25] B. Gysen, E. Lomonova, J. Paulides, A. Vandenput, Analytical and numerical techniques for solving laplace and poisson equations in a tubular permanent magnet actuator: Part ii. schwarz-christoffel mapping, *IEEE Transactions on Magnetics* 44 (7) (2008) 1761–1767.
- [26] Z. Li, L. Wu, Y. Li, Q. Lu, X. Huang, L. Peretti, Y. Shen, Hybrid analytical model of permanent magnet linear motor considering iron saturation and end effect, *IEEE Transactions on Energy Conversion* 39 (3) (2024) 2008–2017. doi:10.1109/tec.2024.3354488.
- [27] Q. Lu, B. Wu, Y. Yao, Y. Shen, Q. Jiang, Analytical model of permanent magnet linear synchronous machines considering end effect and slotting effect, *IEEE Transactions on Energy Conversion* 35 (1) (2020) 139–148. doi:10.1109/tec.2019.2946278.
- [28] E. Furlani, Formulas for the force and torque of axial couplings, *IEEE Transactions on Magnetics* 29 (5) (1993) 2295–2301.
- [29] J. P. Selvaggi, S. J. Salon, M. V. K. Chari, Employing toroidal harmonics for computing the magnetic field from axially magnetized multipole cylinders, *IEEE Transactions on Magnetics* 46 (10) (2010) 3715–3723.
- [30] J. A. Stratton, Electromagnetic theory, 1st Edition, International series in physics, McGraw-Hill, New York, 1941.
- [31] M. Forbes, <https://github.com/AUMAG/mag-gmst-force> (2024).
- [32] C. Custers, J. Jansen, M. van Beurden, E. Lomonova, 3D harmonic modeling of eddy currents in segmented conducting structures, *COMPEL* 38 (1) (2019) 2–23.
- [33] R. Pile, J. Le Besnerais, G. Parent, E. Devillers, T. Henneron, Y. Le Menach, J.-P. Lecointe, Analytical study of air-gap surface force – application to electrical machines, *Open Physics* 18 (1) (2020) 658–673.
- [34] D. Torregrossa, F. Peyrout, B. Fahimi, J. M'Boua, A. Miraoui, Multi-physics finite-element modeling for vibration and acoustic analysis of permanent magnet synchronous machine, *IEEE Transactions on Energy Conversion* 26 (2) (2011) 490–500.
- [35] S. Zuo, F. Lin, X. Wu, Noise analysis, calculation, and reduction of external rotor permanent-magnet synchronous motor, *IEEE Transactions on Industrial Electronics* 62 (10) (2015) 6204–6212.
- [36] Y. Guo, X. Ba, L. Liu, H. Lu, G. Lei, W. Yin, J. Zhu, A review of electric motors with soft magnetic composite cores for electric drives, *Energies* 16 (4) (2023) 2053.
- [37] M. Forbes, W. S. P. Robertson, A. C. Zander, J. J. H. Paulides, Analytic magnetic field modelling approach for iron-less tubular permanent magnet linear synchronous motors, in: 2019 IEEE Energy Conversion Congress and Exposition (ECCE), 2019, pp. 3038–3045. doi:10.1109/ECCE.2019.8912925.
- [38] K. J. Meessen, B. L. J. Gysen, J. J. H. Paulides, E. A. Lomonova, Three-dimensional magnetic field modeling of a cylindrical Halbach array, *IEEE Transactions on Magnetics* 46 (6) (2010) 1733–1736.
- [39] L. Yan, J. Hu, Z. Jiao, I.-M. Chen, C. K. Lim, Magnetic field modeling of linear machines with double-layered halbach arrays, in: Proceedings of 2011 International Conference on Fluid Power and Mechatronics, IEEE, 2011, pp. 1–6.
- [40] L. Yan, L. Zhang, Z. Jiao, H. Hu, C.-Y. Chen, I.-M. Chen, Armature reaction field and inductance of coreless moving-coil tubular linear machine, *IEEE Transactions on Industrial Electronics* 61 (12) (2014) 6956–6965.
- [41] L. Yan, L. Zhang, J. Peng, L. Zhang, Z. Jiao, Electromagnetic Linear Machines with Dual Halbach Array: Design and Analysis, 1st Edition, Springer Singapore, Singapore, 2017.
- [42] B. P. Ruddy, High force density linear permanent magnet motors: “electromagnetic muscle actuators”, Massachusetts Institute of Technology, 2012, phD Thesis.
- [43] B. P. Ruddy, I. W. Hunter, A compact direct-drive linear synchronous motor with muscle-like performance, in: IEEE International Conference on Robotics and Automation, 2013, pp. 1498–1503.
- [44] M. F. J. Kremers, J. J. H. Paulides, J. L. G. Janssen, E. A. Lomonova, Design considerations for coreless linear actuators, *IEEE Transactions on Magnetics* 49 (5) (2013) 2271–2274.
- [45] S. Mohammadi, J. H. Lang, J. L. Kirtley, D. L. Trumper, Modeling and design of a double-sided linear motor with Halbach array for low-vibration and high-acceleration applications, arXiv (Cornell University) (2023).
- [46] D. J. Griffiths, Introduction to electrodynamics, fourth edition, pearson new international edition. Edition, Pearson custom library, Pearson, Harlow, Essex, 2014.
- [47] K. J. Meessen, J. J. H. Paulides, E. A. Lomonova, Modeling and experimental verification of a tubular actuator for 20-g acceleration in a pick-and-place application, *IEEE Transactions on Industry Applications* 46 (5) (2010) 1891–1898.
- [48] P. R. Eckert, A. F. Flores Filho, E. A. Perondi, D. G. Dorrell, Dual quasi-Halbach linear tubular actuator with coreless moving-coil for semiaactive and active suspension, *IEEE Transactions on Industrial Electronics* 65 (12) (2018) 9873–9883.
- [49] K. J. Meessen, J. J. H. Paulides, E. A. Lomonova, Analysis of 3-D effects in segmented cylindrical quasi-Halbach magnet arrays, *IEEE Transactions on Magnetics* 47 (4) (2011) 727–733.
- [50] J. M. D. Coey, Hard magnetic materials: A perspective, *IEEE Transactions on Magnetics* 47 (12) (2011) 4671–4681.
- [51] P. R. Eckert, A. F. F. Filho, E. Perondi, J. Ferri, E. Goltz, Design methodology of a dual-Halbach array linear actuator with thermal-electromagnetic coupling, *Sensors* 16 (3) (2016).
- [52] L. Yan, L. Zhang, L. Peng, Z. Jiao, Comparative study of the dual layer magnet array in a moving-coil tubular linear PM motor, *Sensors* 18 (6) (2018) 1854.
- [53] J. Wang, G. W. Jewell, D. Howe, Design optimisation and comparison of tubular permanent magnet machine topologies, *IEE Proceedings - Electric Power Applications* 148 (5) (2001) 456–464.
- [54] K. Meessen, B. Gysen, J. Paulides, E. Lomonova, Halbach permanent magnet shape selection for slotless tubular actuators, *IEEE Transactions on Magnetics* 44 (11) (2008) 4305–4308.
- [55] J. Wang, D. Howe, G. Jewell, Analysis and design optimization of an improved axially magnetized tubular permanent-magnet machine, *IEEE Transactions on Energy Conversion* 19 (2) (2004) 289–295. doi:10.1109/tec.2004.827026.
- [56] Höganäs, <https://www.hoganas.com/electromagnetic>, accessed: Mar. 01, 2020 (2018).

Appendix A. The generalised Maxwell stress tensor

From [21], the generalised Maxwell stress tensor (GMST) is

$$\mathbf{F}_{\text{GMST}}(\mathbf{B}_E, \mathbf{B}_I) = \oint_{\partial V} \mathcal{F}(\mathbf{B}_E, \mathbf{B}_I) \cdot \mathbf{n} \, ds \quad (\text{A.1})$$

with vector fields $\mathbf{B}_E = B_x^E \mathbf{e}_x + B_y^E \mathbf{e}_y + B_z^E \mathbf{e}_z$ and $\mathbf{B}_I = B_x^I \mathbf{e}_x + B_y^I \mathbf{e}_y + B_z^I \mathbf{e}_z$, outward facing normal \mathbf{n} , and symmetric force tensor

$$\mathcal{F}(\mathbf{B}_E, \mathbf{B}_I) = \frac{1}{\mu_0} \begin{bmatrix} \mathcal{F}_{11} & \mathcal{F}_{12} & \mathcal{F}_{13} \\ \mathcal{F}_{21} & \mathcal{F}_{22} & \mathcal{F}_{23} \\ \mathcal{F}_{31} & \mathcal{F}_{32} & \mathcal{F}_{33} \end{bmatrix},$$

$$\mathcal{F}_{11} = B_x^E B_x^I - B_y^E B_y^I - B_z^E B_z^I,$$

$$\mathcal{F}_{22} = B_y^E B_y^I - B_x^E B_x^I - B_z^E B_z^I,$$

$$\mathcal{F}_{33} = B_z^E B_z^I - B_x^E B_x^I - B_y^E B_y^I,$$

$$\mathcal{F}_{12} = \mathcal{F}_{21} = B_x^E B_y^I + B_y^E B_x^I,$$

$$\mathcal{F}_{13} = \mathcal{F}_{31} = B_x^E B_z^I + B_z^E B_x^I,$$

$$\mathcal{F}_{23} = \mathcal{F}_{32} = B_y^E B_z^I + B_z^E B_y^I.$$

From (A.1) with radius vector $\mathbf{r} = x \mathbf{e}_x + y \mathbf{e}_y + z \mathbf{e}_z$ the GMST torque is

$$\mathbf{T}_{\text{GMST}}(\mathbf{r}, \mathbf{B}_E, \mathbf{B}_I) = \oint_S \mathcal{T}(\mathbf{r}, \mathbf{B}_E, \mathbf{B}_I) \cdot \mathbf{n} \, ds, \quad (\text{A.2})$$

with the torque tensor

$$\mathcal{T}(\mathbf{r}, \mathbf{B}_E, \mathbf{B}_I) = \frac{1}{\mu_0} \begin{bmatrix} \mathcal{T}_{11} & \mathcal{T}_{12} & \mathcal{T}_{13} \\ \mathcal{T}_{21} & \mathcal{T}_{22} & \mathcal{T}_{23} \\ \mathcal{T}_{31} & \mathcal{T}_{32} & \mathcal{T}_{33} \end{bmatrix},$$

$$\mathcal{T}_{11} = y(B_x^E B_z^I - B_z^E B_x^I) - z(B_x^E B_y^I + B_y^E B_x^I),$$

$$\mathcal{T}_{22} = z(B_x^E B_y^I + B_y^E B_x^I) - x(B_y^E B_z^I - B_z^E B_y^I),$$

$$\mathcal{T}_{33} = x(B_y^E B_z^I - B_z^E B_y^I) - y(B_x^E B_z^I + B_z^E B_x^I),$$

$$\mathcal{T}_{12} = y(B_y^E B_z^I + B_z^E B_y^I) + z(B_x^E B_z^I - B_y^E B_y^I + B_z^E B_z^I),$$

$$\mathcal{T}_{13} = -z(B_y^E B_z^I + B_z^E B_y^I) - y(B_x^E B_z^I + B_y^E B_y^I - B_z^E B_z^I),$$

$$\mathcal{T}_{21} = -x(B_x^E B_z^I + B_z^E B_x^I) + z(B_x^E B_z^I - B_y^E B_y^I - B_z^E B_z^I),$$

$$\mathcal{T}_{23} = z(B_x^E B_z^I + B_z^E B_x^I) + x(B_x^E B_z^I + B_y^E B_y^I - B_z^E B_z^I),$$

$$\mathcal{T}_{31} = x(B_x^E B_z^I + B_y^E B_x^I) - y(B_x^E B_z^I - B_y^E B_y^I - B_z^E B_z^I),$$

$$\mathcal{T}_{32} = -y(B_x^E B_z^I + B_y^E B_x^I) - x(B_x^E B_z^I - B_y^E B_y^I + B_z^E B_z^I).$$